

1 SEARCH FOR PRODUCTION OF A HIGGS BOSON AND A SINGLE TOP
2 QUARK IN MULTILEPTON FINAL STATES IN pp COLLISIONS AT $\sqrt{s} = 13$
3 TeV.

4 by

5 Jose Andres Monroy Montañez

6 A DISSERTATION

7 Presented to the Faculty of
8 The Graduate College at the University of Nebraska
9 In Partial Fulfilment of Requirements
10 For the Degree of Doctor of Philosophy

11 Major: Physics and Astronomy

12 Under the Supervision of Kenneth Bloom and Aaron Dominguez

13 Lincoln, Nebraska

14 July, 2018

15 SEARCH FOR PRODUCTION OF A HIGGS BOSON AND A SINGLE TOP
16 QUARK IN MULTILEPTON FINAL STATES IN pp COLLISIONS AT $\sqrt{s} = 13$
17 TeV.

18 Jose Andres Monroy Montañez, Ph.D.
19 University of Nebraska, 2018

20 Adviser: Kenneth Bloom and Aaron Dominguez

²¹ Table of Contents

²²	Table of Contents	iii
²³	List of Figures	v
²⁴	List of Tables	vii
²⁵	1 INTRODUCTION	1
²⁶	2 Theoretical approach	2
²⁷	2.1 Introduction	2
²⁸	2.2 Standard model of particle physics	3
²⁹	2.2.1 Fermions	5
³⁰	2.2.1.1 Leptons	6
³¹	2.2.1.2 Quarks	8
³²	2.2.2 Fundamental interactions	12
³³	2.2.3 Gauge bosons	18
³⁴	2.3 Electroweak unification and the Higgs mechanism	20
³⁵	2.3.1 Spontaneous symmetry breaking (SSB)	28
³⁶	2.3.2 Higgs mechanism	32
³⁷	2.3.3 Masses of the gauge bosons	34

38	2.3.4	Masses of the fermions	35
39	2.3.5	The Higgs field	36
40	2.3.6	Production of Higgs bosons at LHC	37
41	2.3.7	Higgs boson decay channels	41
42	2.4	Associated production of a Higgs boson and a single Top quark.	42
43	2.5	The CP-mixing in tH processes	47
44	2.6	Experimantal status of the anomalous Higg-fermion coupling.	51
45	3	The CMS experiment at the LHC	53
46	3.1	Introduction	53
47	3.2	The LHC	54
48	3.3	The CMS experiment	63
49	3.3.1	Coordinate system	65
50	3.3.2	Pixels detector	67
51	3.3.3	Silicon strip tracker	69
52	3.3.4	Electromagnetic calorimeter	70
53	3.3.5	Hadronic calorimeter	72
54	3.3.6	Superconducting solenoid magnet	73
55	3.3.7	Muon system	75
56	3.3.8	CMS trigger system	76
57	3.3.9	CMS computing	78
58	Bibliography		80
59	References		82

⁶⁰ List of Figures

61	2.1	Standard model of particle physics.	4
62	2.2	Transformations between quarks	12
63	2.3	Fundamental interactions in nature.	13
64	2.4	SM interactions diagrams	14
65	2.5	Neutral current processes	21
66	2.6	Spontaneous symmetry breaking mechanism	28
67	2.7	SSB Potential form	29
68	2.8	Potential for complex scalar field	30
69	2.9	SSB mechanism for complex scalar field	31
70	2.10	Proton-Proton collision	38
71	2.11	Higgs boson production mechanism Feynman diagrams	39
72	2.12	Higgs boson production cross section and decay branching ratios	40
73	2.13	Associated Higgs boson production mechanism Feynman diagrams	43
74	2.14	Cross section for tHq process as a function of κ_t	45
75	2.15	Cross section for tHW process as a function of κ_{Htt}	46
76	2.16	NLO cross section for tX_0 and $t\bar{t}X_0$.	49
77	2.17	NLO cross section for tWX_0 , $t\bar{t}X_0$.	50

78	2.18 Two dimentional κ_t - κ_V plot of the coupling modifiers. ATLAS and CMS 79 combination.	51
80	3.1 CERN accelerator complex	54
81	3.2 LHC protons source. First acceleration stage.	55
82	3.3 The LINAC2 accelerating system at CERN.	56
83	3.4 LHC layout and RF cavities module.	57
84	3.5 LHC dipole magnet.	59
85	3.6 Integrated luminosity delivered by LHC and recorded by CMS during 2016	61
86	3.7 LHC interaction points	62
87	3.8 Multiple pp collision bunch crossing at CMS.	64
88	3.9 Layout of the CMS detector	65
89	3.10 CMS detector coordinate system	66
90	3.11 CMS pixel detector schematic view.	68
91	3.12 SST Schematic view.	69
92	3.13 CMS ECAL schematic view	71
93	3.14 CMS HCAL schematic view	72
94	3.15 CMS solenoid magnet	74
95	3.16 CMS Muon system schematic view	75
96	3.17 CMS Level-1 trigger architecture	77
97	3.18 WLCG structure	78
98	3.19 Data flow from CMS detector through hardware Tiers	81

⁹⁹ List of Tables

100	2.1	Fermions of the SM.	5
101	2.2	Fermion masses.	6
102	2.3	Leptons properties.	9
103	2.4	Quarks properties.	9
104	2.5	Fermion weak isospin and weak hypercharge multiplets.	11
105	2.6	Fundamental interactions features.	15
106	2.7	SM gauge bosons.	19
107	2.8	Higgs boson properties.	37
108	2.9	Predicted branching ratios for a SM Higgs boson with $m_H = 125 \text{ GeV}/c^2$	42
109	2.10	Predicted SM cross sections for tH production at $\sqrt{s} = 13 \text{ TeV}$	44
110	2.11	Predicted enhancement of the tHq and tHW cross sections at LHC	47

¹¹¹ Chapter 1

¹¹² INTRODUCTION

¹¹³ **Chapter 2**

¹¹⁴ **Theoretical approach**

¹¹⁵ **2.1 Introduction**

¹¹⁶ The physical description of the universe is a challenge that physicists have faced by
¹¹⁷ making theories that refine existing principles and proposing new ones in an attempt
¹¹⁸ to embrace emerging facts and phenomena.

¹¹⁹

¹²⁰ At the end of 1940s Julian Schwinger [1] and Richard P. Feynman [2], based in the
¹²¹ work of Sin-Itiro Tomonaga [3], developed an electromagnetic theory consistent with
¹²² special relativity and quantum mechanics that describes how matter and light inter-
¹²³ act; the so-called “quantum eletrodynamics” (QED) had born.

¹²⁴

¹²⁵ QED has become the guide in the development of theories that describe the universe.
¹²⁶ It was the first example of a quantum field theory (QFT), which is the theoretical
¹²⁷ framework for building quantum mechanical models that describes particles and their
¹²⁸ interactions. QFT is composed of a set of mathematical tools that combines classical
¹²⁹ fields, special relativity and quantum mechanics, while keeping the quantum point

130 particles and locality ideas.

131 This chapter gives an overview of the standard model of particle physics, starting
 132 with a description of the particles and interactions that compose it, followed by a
 133 description of the electroweak interaction, the Higgs boson and the associated pro-
 134 duction of Higgs boson and a single top quark (tH). The description contained in
 135 this chapter is based on references [4–6].

136 2.2 Standard model of particle physics

137 Particle physics at the fundamental level is modeled in terms of a collection of in-
 138 teracting particles and fields in a theory known as the “standard model of particle
 139 physics (SM)”¹.

140

141 The full picture of the SM is composed of three fields², whose excitations are inter-
 142 preted as particles called mediators or force-carriers; a set of fields, whose excitations
 143 are interpreted as elementary particles, interacting through the exchange of those
 144 mediators and a field that gives the mass to elementary particles. Figure 2.1 shows
 145 an scheme of the SM particles organization. In addition to the particles in the scheme
 146 (but not listed in it), their corresponding anti-particles, with opposite quantum num-
 147 bers, are also part of the picture; some particles are their own anti-particles, like
 148 photon or Higgs, or anti-particle is already listed like in the W^+ and W^- case.

149

150 The mathematical formulation of the SM is based on group theory and the use of
 151 Noether’s theorem [8] which states that for a physical system modeled by a Lagrangian

¹ The formal and complete treatment of the SM is out of the scope of this document, however a plenty of textbooks describing it at several levels are available in the literature. The treatment in references [?] is quite comprehensive and detailed.

² Note that gravitational field is not included in the standard model formulation

Standard Model of Elementary Particles

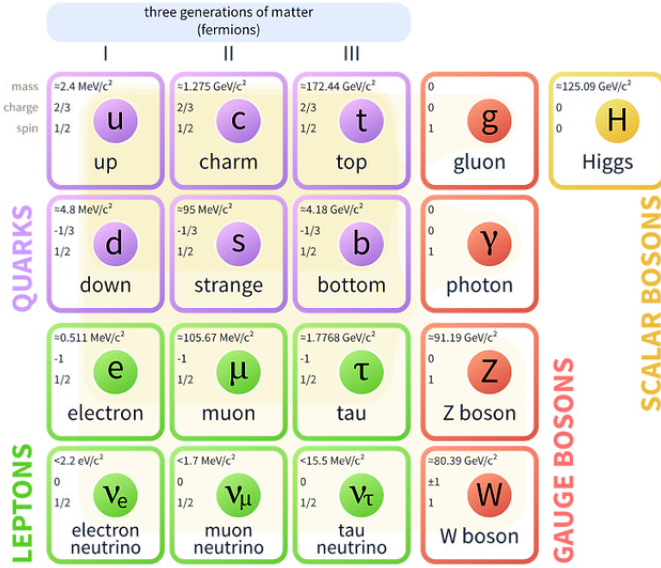


Figure 2.1: Schematic representation of the Standard model of particle physics. SM is a theoretical model intended to describe three of the four fundamental forces of the universe in terms of a set of particles and their interactions. [7].

that is invariant under a group of transformations a conservation law is expected. For instance, a system described by a time-independent Lagrangian is invariant (symmetric) under time changes (transformations) with the total energy conservation law as the expected conservation law. In QED, the charge operator (Q) is the generator of the $U(1)$ symmetry which according to the Noether's theorem means that there is a conserved quantity; this conserved quantity is the electric charge and thus the law of conservation of electric charge is established.

159

In the SM, the symmetry group $SU(3)_C \otimes SU(2)_L \otimes U(1)_Y$ describes three of the four fundamental interactions in nature(see section 2.2.2): strong interaction(SI), weak interaction(WI) and electromagnetic interactions (EI) in terms of symmetries associated to physical quantities:

- 164 • Strong: $SU(3)_C$ associated to color charge
- 165 • Weak: $SU(2)_L$ associated to weak isospin and chirality
- 166 • Electromagnetic: $U(1)_Y$ associated to weak hypercharge and electric charge
- 167 It will be shown that the electromagnetic and weak interactions are combined in
 168 the so-called electroweak interaction where chirality, hypercharge, weak isospin and
 169 electric charge are the central concepts.

170 **2.2.1 Fermions**

171 The basic constituents of the ordinary matter at the lowest level, which form the set
 172 of elementary particles in the SM formulation, are quarks and leptons. All of them
 173 have spin 1/2, therefore they are classified as fermions since they obey Fermi-Dirac
 174 statistics. There are six “flavors” of quarks and three of leptons organized in three
 175 generations, or families, as shown in table 2.1.

176

		Generation		
		1st	2nd	3rd
Leptons	Type	Electron (e)	Moun(μ)	Tau (τ)
	Charged Neutral	Electron neutrino (ν_e)	Muon neutrino (ν_μ)	Tau neutrino (ν_τ)
Quarks	Up-type	Up (u)	Charm (c)	Top (t)
	Down-type	Down (d)	Strange (s)	Bottom (b)

Table 2.1: Fermions of the SM. There are six flavors of quarks and three of leptons, organized in three generations, or families, composed of two pairs of closely related particles. The close relationship is motivated by the fact that WI between leptons is limited to the members of the same generation; WI between quarks is not limited but greatly favoured, to same generation members.

177

178 There is a mass hierarchy between generations (see table 2.2), where the higher gener-
 179 ation particles decays to the lower one, which can explain why the ordinary matter is

made of particles in the first generation. In the SM, neutrinos are modeled as massless particles so they are not subject to this mass hierarchy; however, today it is known that neutrinos are massive so the hierarchy could be restated. The reason behind this mass hierarchy is one of the most important open questions in particle physics, and it becomes more puzzling when noticing that the mass difference between first and second generation fermions is small compared to the mass difference with respect to the third generation.

Lepton	Mass (MeV/c ²)	Quark	Mass (MeV/c ²)
e	0.51	u	2.2
μ	105.65	c	1.28×10^3
τ	1776.86	t	173.1×10^3
ν_e	Unknown	d	4.7
ν_μ	Unknown	s	96
τ_μ	Unknown	b	4.18×10^3

Table 2.2: Fermion masses [9]. Generations differ by mass in a way that have been interpreted as a masss hierarchy. Approximate values with no uncertainties are used, for comparison purpose.

187

Usually, the second and third generation fermions are produced in high energy processes, like the ones recreated in particle accelerators.

190 2.2.1.1 Leptons

A lepton is an elementary particle that is not subject to the SI. As seen in table 2.1, there are two types of leptons, the charged ones (electron, muon and tau) and the neutral ones (the three neutrinos). The electric charge (Q) is the property that gives leptons the ability to participate in the EI. From the classical point of view, Q plays a central role determining, among others, the strength of the electric field through which the electromagnetic force is exerted. It is clear that neutrinos are not affected

197 by EI because they don't carry electric charge.

198

199 Another feature of the leptons that is fundamental in the mathematical description
200 of the SM is the chirality, which is closely related to spin and helicity. Helicity defines
201 the handedness of a particle by relating its spin and momentum such that if they
202 are parallel then the particle is right-handed; if spin and momentum are antiparallel
203 the particle is said to be left-handed. The study of parity conservation (or viola-
204 tion) in β -decay has shown that only left-handed electrons/neutrinos or right-handed
205 positrons/anti-neutrinos are created [10]; the inclusion of that feature in the theory
206 was achieved by using projection operators for helicity, however, helicity is frame de-
207 pendent for massive particles which makes it not Lorentz invariant and then another
208 related attribute has to be used: *chirality*.

209

210 Chirality is a purely quantum attribute which makes it not so easy to describe in
211 graphical terms but it defines how the wave function of a particle transforms under
212 certain rotations. As with helicity, there are two chiral states, left-handed chiral (L)
213 and right-handed chiral (R). In the highly relativistic limit where $E \approx p \gg m$ helicity
214 and chirality converge, becoming exactly the same for massless particles.

215

216 In the following, when referring to left-handed (right-handed) it will mean left-handed
217 chiral (right-handed chiral). The fundamental fact about chirality is that while EI
218 and SI are not sensitive to chirality, in WI left-handed and right-handed fermions are
219 treated asymmetrically, such that only left handed fermions and right-handed anti-
220 fermions are allowed to couple to WI mediators, which is a violation of parity. The
221 way to translate this statement in a formal mathematical formulation is based on the
222 isospin symmetry group $SU(2)_L$.

223

224 Each generation of leptons is seen as a weak isospin doublet.³ The left-handed charged
 225 lepton and its associated left-handed neutrino are arranged in doublets of weak isospin
 226 T=1/2 while their right-handed partners are singlets:

$$\begin{pmatrix} \nu_l \\ l \end{pmatrix}_L, l_R := \begin{pmatrix} \nu_e \\ e \end{pmatrix}_L, \begin{pmatrix} \nu_\mu \\ \mu \end{pmatrix}_L, \begin{pmatrix} \nu_\tau \\ \tau \end{pmatrix}_L, e_R, \mu_R, \tau_R, \nu_{eR}, \nu_{\mu R}, \nu_{\tau R} \quad (2.1)$$

227 The isospin third component refers to the eigenvalues of the weak isospin operator
 228 which for doublets is $T_3 = \pm 1/2$, while for singlets it is $T_3 = 0$. The physical meaning
 229 of this doublet-singlet arrangement falls in that the WI couples the two particles in
 230 the doublet by exchanging the interaction mediator while the singlet member is not
 231 involved in WI. The main properties of the leptons are summarized in table 2.3.

232

233 Altough all three flavor neutrinos have been observed, their masses remain unknown
 234 and only some estimations have been made [11]. The main reason is that the fla-
 235 vor eigenstates are not the same as the mass eigenstates which implies that when
 236 a neutrino is created its mass state is a linear combination of the three mass eigen-
 237 states and experiments can only probe the squared difference of the masses. The
 238 Pontecorvo-Maki-Nakagawa-Sakata (PMNS) mixing matrix encode the relationship
 239 between flavor and mass eigenstates.

240

241 2.2.1.2 Quarks

242 Quarks are the basic constituents of protons and neutrons. The way quarks join to
 243 form bound states, called “hadrons”, is through the SI. Quarks are affected by all the

³ The weak isospin is an analogy of the isospin symmetry in strong interaction where neutron and proton are affected equally by strong force but differ in their charge.

Lepton	Q(e)	T_3	L_e	L_μ	L_τ	Lifetime (s)
Electron (e)	-1	-1/2	1	0	0	Stable
Electron neutrino(ν_e)	0	1/2	1	0	0	Unknown
Muon (μ)	-1	-1/2	0	1	0	2.19×10^{-6}
Muon neutrino (ν_μ)	0	1/2	0	1	0	Unknown
Tau (τ)	-1	-1/2	0	0	1	290.3×10^{-15}
Tau neutrino (τ_μ)	0	1/2	0	0	1	Unknown

Table 2.3: Leptons properties [9]. Q: electric charge, T_3 : weak isospin. Only left-handed leptons and right-handed anti-leptons participate in the WI. Anti-particles with inverted T_3 , Q and lepton number complete the leptons set but are not listed. Right-handed leptons and left-handed anti-leptons, neither listed, form weak isospin singlets with $T_3 = 0$ and do not take part in the weak interaction.

244 fundamental interactions which means that they carry all the four types of charges:
 245 color, electric charge, weak isospin and mass.

Flavor	Q(e)	I_3	T_3	B	C	S	T	B'	Y	Color
Up (u)	2/3	1/2	1/2	1/3	0	0	0	0	1/3	r,b,g
Charm (c)	2/3	0	1/2	1/3	1	0	0	0	4/3	r,b,g
Top(t)	2/3	0	1/2	1/3	0	0	1	0	4/3	r,b,g
Down(d)	-1/3	-1/2	-1/2	1/3	0	0	0	0	1/3	r,b,g
Strange(s)	-1/3	0	-1/2	1/3	0	-1	0	0	-2/3	r,b,g
Bottom(b)	-1/3	0	-1/2	1/3	0	0	0	-1	-2/3	r,b,g

Table 2.4: Quarks properties [9]. Q: electric charge, I_3 : isospin, T_3 : weak isospin, B: baryon number, C: charmness, S: strangeness, T: topness, B' : bottomness, Y: hypercharge. Anti-quarks posses the same mass and spin as quarks but all charges (color, flavor numbers) have opposite sign.

246
 247 Table 2.4 summarizes the features of quarks, among which the most particular is
 248 their fractional electric charge. Note that fractional charge is not a problem, given
 249 that quarks are not found isolated, but serves to explain how composed particles are
 250 formed out of two or more valence quarks⁴.

251

⁴ Hadrons can contain an indefinite number of virtual quarks and gluons, known as the quark and gluon sea, but only the valence quarks determine hadrons' quantum numbers.

252 Color charge is the responsible for the SI between quarks and is the symmetry
 253 ($SU(3)_C$) that defines the formalism to describe SI. There are three colors: red (r),
 254 blue(b) and green(g) and their corresponding three anti-colors; thus each quark carries
 255 one color unit while anti-quarks carries one anti-color unit. As said above, quarks are
 256 not allowed to be isolated due to the color confinement effect, therefore their features
 257 have been studied indirectly by observing their bound states created when:

- 258 • one quark with a color charge is attracted by an anti-quark with the correspond-
 259 ing anti-color charge forming a colorless particle called a “meson.”
- 260 • three quarks (anti-quarks) with different color (anti-color) charges are attracted
 261 among them forming a colorless particle called a “baryon(anti-baryon).”

262 In the first version of the quark model (1964), M. Gell-Mann [12] and G. Zweig
 263 [13, 14] developed a consistent way to classify hadrons according to their properties.
 264 Only three quarks (u, d, s) were involved in a scheme in which all baryons have
 265 baryon number $B=1$ and therefore quarks have $B=1/3$; non-baryons have $B=0$. The
 266 scheme organizes baryons in a two-dimensional space ($I_3 - Y$); Y (hypercharge) and I_3
 267 (isospin) are quantum numbers related by the Gell-Mann-Nishijima formula [15, 16]:

$$Q = I_3 + \frac{Y}{2} \quad (2.2)$$

268 where $Y = B + S + C + T + B'$ are the quantum numbers listed in table 2.4. Baryon
 269 number is conserved in SI and EI which means that single quarks cannot be created
 270 but in pairs $q - \bar{q}$.

271

272 There are six quark flavors organized in three generations (see table 2.1) following a
 273 mass hierarchy which, again, implies that higher generations decay to first generation

274 quarks.

	Quarks			T_3	Y_W	Leptons			T_3	Y_W
Doublets	$(\frac{u}{d'})_L$	$(\frac{c}{s'})_L$	$(\frac{t}{b'})_L$	$(\frac{1/2}{-1/2})$	$1/3$	$(\nu_e)_L$	$(\nu_\mu)_L$	$(\nu_\tau)_L$	$(\frac{1/2}{-1/2})$	-1
Singlets	u_R	c_R	t_R	0	$4/3$	ν_{eR}	$\nu_{\mu R}$	$\nu_{\tau R}$	0	-2
	d'_R	s'_R	b'_R	0	$-2/3$	e_R	μ_R	τ_R		

Table 2.5: Fermion weak isospin and weak hypercharge multiplets. Weak hypercharge is calculated through the Gell-Mann-Nishijima formula 2.2 but using the weak isospin and charge for quarks.

275

276 Isospin doublets of quarks are also defined (see table 2.5) and as for neutrinos, the
 277 mass eigenstates are not the same as the WI eigenstates which means that members of
 278 different quark generations are connected by the WI mediator; thus, up-type quarks
 279 are coupled not to down-type quarks directly but to a superposition of down-type
 280 quarks (q'_d) via WI according to:

$$q'_d = V_{CKM} q_d$$

281

$$\begin{pmatrix} d' \\ s' \\ b' \end{pmatrix} = \begin{pmatrix} V_{ud} & V_{us} & V_{ub} \\ V_{cd} & V_{cs} & V_{cb} \\ V_{td} & V_{ts} & V_{tb} \end{pmatrix} \begin{pmatrix} d \\ s \\ b \end{pmatrix} \quad (2.3)$$

282 where V_{CKM} is known as Cabibbo-Kobayashi-Maskawa (CKM) mixing matrix [17,18].
 283 The weak decays of quarks are represented in the diagram of figure 2.2; again the
 284 CKM matrix plays a central role since it contains the probabilities for the different
 285 quark decay channels, in particular, note that quark decays are greatly favored be-
 286 tween generation members.

287

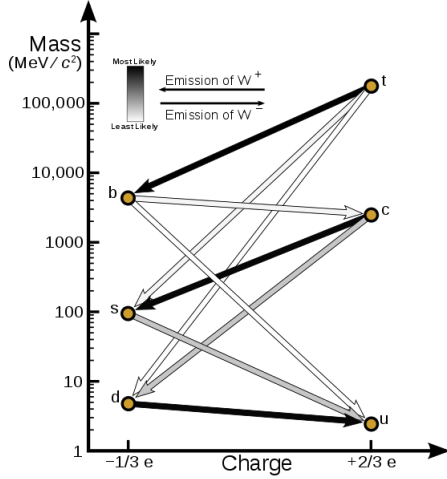


Figure 2.2: Transformations between quarks through the exchange of a WI. Higher generations quarks decay to first generation quarks by emitting a W boson. The arrow color indicates the likelihood of the transition according to the grey scale in the top left side which represent the CKM matrix parameters [19].

288 CKM matrix is a 3×3 unitary matrix parametrized by three mixing angles and
 289 the *CP-mixing phase*; the latter is the parameter responsible for the Charge-Parity
 290 symmetry violation (CP-violation) in the SM. The fact that the b quark decays almost
 291 all the times to a top quark is exploited in this thesis when making the selection of
 292 the signal events by requiring the presence of a jet tagged as a jet coming from a
 293 b quark in the final state. The effect of the *CP-mixing phase* on the cross section of
 294 associated production of Higgs boson and a single top process is also explored in this
 295 thesis.

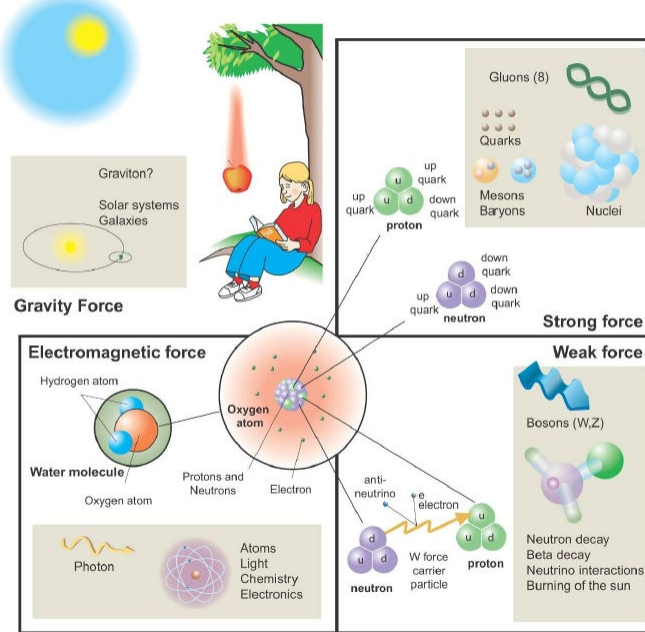
296 2.2.2 Fundamental interactions

297 Even though there are many manifestations of force in nature, like the ones repre-
 298 sented in figure 2.3, we can classify all of them into one of four fundamental interac-
 299 tions:

- 300 • *Electromagnetic interaction (EI)* affects particles that are “electrically charged,”

Fundamental interactions.

Illustration: Typoform



Summer School KPI 15 August 2009

Figure 2.3: Fundamental interactions in nature. Despite the many manifestations of forces in nature, we can track all of them back to one of the fundamental interactions. The most common forces are gravity and electromagnetic given that all of us are subject and experience them in everyday life.

301 like electrons and protons. It is described by QED combining quantum mechan-
 302 ics, special relativity and electromagnetism in order to explain how particles
 303 with electric charge interact through the exchange of photons, therefore, one
 304 says that “Electromagnetic Force” is mediated by “photons”. Figure 2.4a. shows
 305 a graphical representation, known as “feynman diagram”, of electron-electron
 306 scattering.

- 307 • *Strong interaction (SI)* described by Quantum Chromodynamics (QCD). Hadrons
 308 like proton and neutron have internal structure given that they are composed
 309 of two or more valence quarks⁵. Quarks have fractional electric charge which
 310 means that they are subject to electromagnetic interaction and in the case of the

⁵ particles made of four and five quarks are exotic states not so common.

311 proton they should break apart due to electrostatic repulsion; however, quarks
 312 are held together inside the hadrons against their electrostatic repulsion by the
 313 “Strong Force” through the exchange of “gluons.” The analog to the electric
 314 charge is the “color charge”. Electrons and photons are elementary particles
 315 as quarks but they don’t carry color charge, therefore they are not subject to
 316 SI. The feynman diagram for gluon exchange between quarks is shown in figure
 317 2.4b.

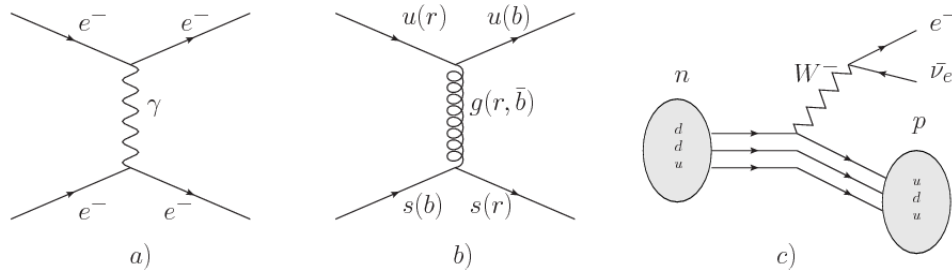


Figure 2.4: Feynman diagrams representing the interactions in SM; a) EI: e - e scattering; b) SI: gluon exchange between quarks ; c) WI: β -decay

318 • *Weak interaction (WI)* described by the weak theory (WT), is responsible, for
 319 instance, for the radioactive decay in atoms and proton-proton (pp) fusion
 320 within the sun. Quarks and leptons are the particles affected by the weak
 321 interaction; they possess a property called “flavor charge” (see 2.2.1) which can
 322 be changed by emitting or absorbing one weak force mediator. There are three
 323 mediators of the “weak force” known as “Z” boson in the case of electrically
 324 neutral changes and “ W^\pm ” bosons in the case of electrically charged changes.
 325 The “weak isospin” is the WI analog to electric charge in EI, and color charge
 326 in SI, and defines how quarks and leptons are affected by the weak force. Figure
 327 2.4c. shows the feynman diagram of β -decay where a newtron (n) is transformed
 328 in a proton (p) by emmiting a W^- particle. Since this thesis is in the frame
 329 of the electroweak interaction, a more detailed description of it will be given in

330 section 2.3

- 331 • *Gravitational interaction (GI)* described by General Theory of Relativity (GR).
 332 It is responsible for the structure of galaxies and black holes as well as the
 333 expansion of the universe. As a classical theory, in the sense that it can be for-
 334 mulated without even appeal to the concept of quantization, it implies that the
 335 spacetime is a continuum and predictions can be made without limitation to the
 336 precision of the measurement tools. The latter represent a direct contradiction
 337 of the quantum mechanics principles. Gravity is deterministic while quantum
 338 mechanics is probabilistic; despite that, efforts to develop a quantum theory of
 339 gravity have predicted the “graviton” as mediator of the Gravitational force⁶.

Interaction	Acts on	Relative strength	Range (m)	Mediators
Electromagnetic (QED)	Electrically charged particles	10^{-2}	Infinite	Photon
Strong (QCD)	Quarks and gluons	1	10^{-15}	Gluon
Weak (WI)	Leptons and quarks	10^{-6}	10^{-18}	W^\pm, Z
Gravitational (GI)	Massive particles	10^{-39}	Infinite	Graviton

Table 2.6: Fundamental interactions features [20].

340

341 Table 2.6 summarizes the main features of the fundamental interactions. The rela-
 342 tive strength of the fundamental forces reveals the meaning of strong and weak; in
 343 a context where the relative strength of the SI is 1, the EI is about hundred times
 344 weaker and WI is about million times weaker than the SI. A good description on
 345 how the relative strength and range of the fundamental interactions are calculated
 346 can be found in references [20, 21]. In the everyday life, only EI and GI are explicitly
 347 experienced due to the range of these interactions; i.e., at the human scale distances

⁶ Actually a wide variety of theories have been developed in an attempt to describe gravity; some famous examples are string theory and supergravity.

348 only EI and GI have appreciable effects, in contrast to SI which at distances greater
 349 than 10^{-15} m become negligible.

350

351 QED was built successfully on the basis of the classical electrodynamics theory (CED)
 352 of Maxwell and Lorentz, following theoretical and experimental requirements imposed
 353 by

- 354 • lorentz invariance: independence on the reference frame.
- 355 • locallity: interacting fields are evaluated at the same space-time point to avoid
 356 action at a distance.
- 357 • renormalizability: physical predictions are finite and well defined
- 358 • particle spectrum, symmetries and conservation laws already known must emerge
 359 from the theory.
- 360 • gauge invariance.

361 The gauge invariance requirement reflects the fact that the fundamental fields cannot
 362 be directly measured but associated fields which are the observables. Electric (“**E**”)
 363 and magnetic (“**B**”) fields in CED are associated with the electric scalar potential
 364 “**V**” and the vector potential “**A**”. In particular, **E** can be obtained by measuring
 365 the change in the space of the scalar potential (ΔV); however, two scalar potentials
 366 differing by a constant “f” correspond to the same electric field. The same happens in
 367 the case of the vector potential “**A**”; thus, different configurations of the associated
 368 fields result in the same set of values of the observables. The freedom in choosing
 369 one particular configuration is known as “gauge freedom”; the transformation law con-
 370 necting two configurations is known as “gauge transformation” and the fact that the

371 observables are not affected by a gauge transformation is called “gauge invariance”.

372

373 When the gauge transformation:

$$\begin{aligned}\mathbf{A} &\rightarrow \mathbf{A} - \nabla f \\ V &\rightarrow V - \frac{\partial f}{\partial t}\end{aligned}\tag{2.4}$$

374 is applied to Maxwell equations, they are still satisfied and the fields remain invariant.

375 Thus, CED is invariant under gauge transformations and is called a “gauge theory”.

376 The set of all gauge transformations form the “symmetry group” of the theory, which

377 according to the group theory, has a set of “group generators”. The number of group

378 generators determine the number of “gauge fields” of the theory.

379

380 As mentioned in the first lines of section 2.2, QED has one symmetry group ($U(1)$)

381 with one group generator (the Q operator) and one gauge field (the electromagnetic

382 field A^μ). In CED there is not a clear definition, beyond the historical convention, of

383 which fields are the fundamental and which are the associated, but in QED it is clear

384 that the fundamental field is A^μ . When a gauge theory is quantized, the gauge field

385 is quantized and its quanta is called “gauge boson”. The word boson characterizes

386 particles with integer spin which obvey Bose-einstein statistics.

387

388 As will be detailed in section 2.3, interactions between particles in a system can be

389 obtained by considering first the Lagrangian density of free particles in the system,

390 which of course is incomplete because the interaction terms have been left out, and

391 demanding global phase transformation invariance. Global phase transformation in-

392 variance means that a gauge transformation is performed identically to every point
 393 in the space⁷ and the Lagrangian remains invariant. Then, the global transformation
 394 is promoted to a local phase transformation (this time the gauge transformation de-
 395 pends on the position in space) and again invariance is required.

396

397 Due to the space dependence of the local tranformation, the Lagrangian density is
 398 not invariant anymore. In order to restate the gauge invariance, the gauge covariant
 399 derivative is introduced in the Lagrangian and with it the gauge field responsible for
 400 the interaction between particles in the system. The new Lagrangian density is gauge
 401 invariant, includes the interaction terms needed to account for the interactions and
 402 provides a way to explain the interaction between particles through the exchange of
 403 the gauge boson.

404 This recipe was used to build QED and the theories that aim to explain the funda-
 405 mental interactions.

406 **2.2.3 Gauge bosons**

407 The importance of the gauge bosons comes from the fact that they are the force
 408 mediators or force carriers. The features of the gauge bosons reflect those of the
 409 fields they represent and they are extracted from the Lagrangian density used to
 410 describe the interactions. In section 2.3, it will be shown how the gauge bosons of the
 411 EI and WI emerge from the electroweak Lagrangian. The SI gauge bosons features
 412 are also extracted from the SI Lagrangian but it is not detailed in this document. The
 413 main features of the SM gauge bosons will be briefly presented below and summarized
 414 in table 2.7.

⁷ Here space corresponds to the 4-dimensional space i.e. space-time.

- 415 • **Photon.** EI occurs when the photon couples to (is exchanged between) particles
 416 carrying electric charge; however, the photon itself does not carry electric charge,
 417 therefore, there is no coupling between photons. Given that the photon is
 418 massless the EI is of infinite range, i.e., electrically charged particles interact
 419 even if they are located far away one from each other; this also implies that
 420 photons always move with the speed of light.
- 421 • **Gluon.** SI is mediated by gluons which, same as photons, are massless. They
 422 carry one unit of color charge and one unit of anticolor charge which means that
 423 gluons couple to other gluons. As a result, the range of the SI is not infinite
 424 but very short due to the attraction between gluons, giving rise to the “color
 425 confinement” which explains why color charged particles cannot be isolated but
 426 live within composited particles, like quarks inside protons.
- 427 • **W, Z.** The WI mediators, W^\pm and Z, are massive which explains their short-
 428 range. Given that the WI is the only interaction that can change the flavor
 429 of the interacting particles, the W boson is the responsible for the nuclear
 430 transmutation where a neutron is converted in a proton or vice versa with the
 431 involvement of an electron and a neutrino (see figure 2.4c). The Z boson is the
 432 responsible of the neutral weak processes like neutrino elastic scattering where
 433 no electric charge but momentum transference is involved. WI gauge bosons
 434 carry isospin charge which makes possible the interaction between them.

Interaction	Mediator	Electric charge (e)	Color charge	Weak Isospin	mass (GeV/c ²)
Electromagnetic	Photon (γ)	0	No	0	0
Strong	Gluon (g)	0	Yes -octet	No	0
Weak	W^\pm	± 1	No	± 1	80.385 ± 0.015
	Z	0	No	0	91.188 ± 0.002

Table 2.7: SM gauge bosons main features [9].

436 2.3 Electroweak unification and the Higgs

437 mechanism

438 Physicists dream of building a theory that contains all the interactions in one single
 439 interaction, i.e., showing that at some scale in energy all the four fundamental in-
 440 teractions are unified and only one interaction emerges in a “Theory of everything”.
 441 The first sign of the feasibility of such unification comes from success in the con-
 442 struction of the CED. Einstein spent years trying to reach that dream, which by
 443 1920 only involved electromagnetism and gravity, with no success; however, a new
 444 partial unification was achieved in the 1960’s, when S.Glashow [22], A.Salam [23] and
 445 S.Weinberg [24] independently proposed that electromagnetic and weak interactions
 446 are two manifestations of a more general interaction called “electroweak interaction
 447 (EWT)”. Both, QCD and EWT, were developed in parallel and following the useful
 448 prescription provided by QED and the gauge invariance principles.

449

450 The theory of weak interactions was capable of explaining the β -decay and in general
 451 the processes mediated by W^\pm bosons. However, there were some processes like the
 452 “ $\nu_\mu - e$ scattering” which would require the exchange of two W bosons (see figure 2.5
 453 top diagrams) giving rise to divergent loop integrals and then non finite predictions.
 454 By including neutral currents involving fermions via the exchange of neutral bosons
 455 Z, those divergences are compensated and the predictions become realistic.

456

457 Neutral weak interaction vertices conserve flavor in the same way as the electromag-
 458 netic vertices do, but additionally, the Z boson can couple to neutrinos which implies
 459 that processes involving charged fermions can proceed through EI or WI but processes
 460 involving neutrinos can proceed only through WI.

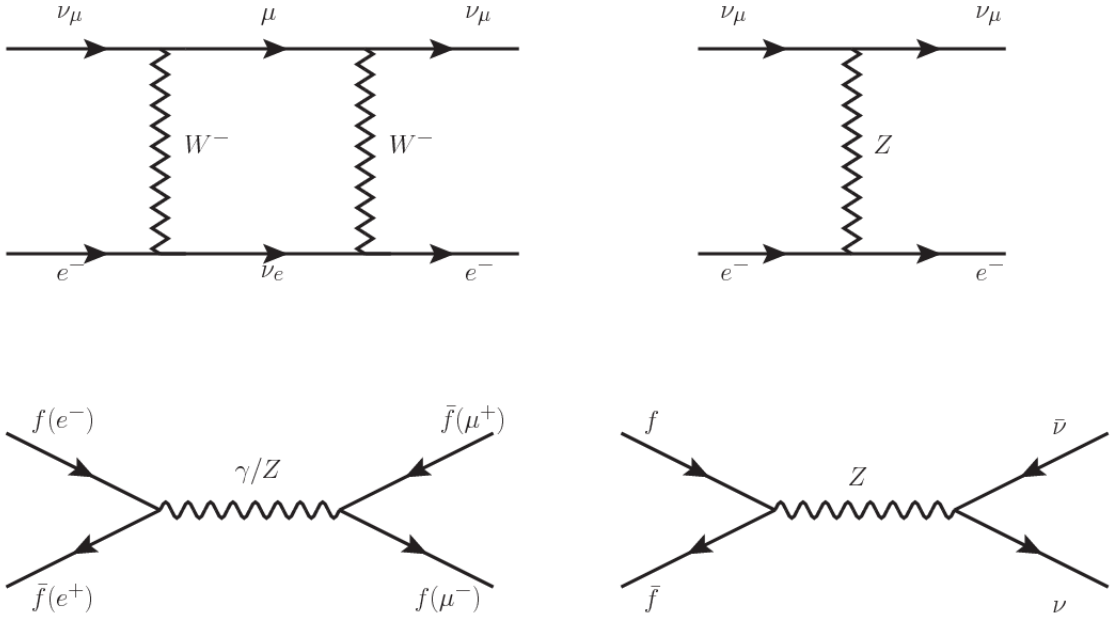


Figure 2.5: Top: $\nu_\mu - e^-$ scattering going through charged currents (left) and neutral currents (right). Bottom: neutral current processes for charged fermions (left) and involving neutrinos (right). While neutral current processes involving only charged fermions can proceed through EI or WI, those involving neutrinos can only proceed via WI.

461

462 The prescription to build a gauge theory of the WI consists of proposing a free field
 463 Lagrangian density that includes the particles involved; next, by requesting invari-
 464 ance under global phase transformations first and generalizing to local phase trans-
 465 formations invariance later, the conserved currents are identified and interactions are
 466 generated by introducing gauge fields. Given that the goal is to include the EI and
 467 WI in a single theory, the group symmetry considered should be a combination of
 468 $SU(2)_L$ and $U(1)_{em}$, however the latter cannot be used directly because the EI treats
 469 left and right-handed particles indistinctly in contrast to the former. Fortunately, the
 470 weak hypercharge, which is a combination of the weak isospin and the electric charge
 471 (eqn 2.2) is suitable to be used since it is conserved by the EI and WI. Thus, the
 472 symmetry group to be considered is

$$G \equiv SU(2)_L \otimes U(1)_Y \quad (2.5)$$

473 The following treatment applies to any of the fermion generations, but for simplicity
 474 the first generation of leptons will be considered [5, 6, 25, 26].

475

476 Given the first generation of leptons

$$\psi_1 = \begin{pmatrix} \nu_e \\ e^- \end{pmatrix}_L, \quad \psi_2 = \nu_{eR}, \quad \psi_3 = e_R^- \quad (2.6)$$

477 the charged fermionic currents are given by

$$J_\mu \equiv J_\mu^+ = \bar{\nu}_{eL} \gamma_\mu e_L, \quad J_\mu^\dagger \equiv J_\mu^- = \bar{e}_L \gamma_\mu \nu_{eL} \quad (2.7)$$

478 and the free Lagrangian is given by

$$\mathcal{L}_0 = \sum_{j=1}^3 i\bar{\psi}_j(x) \gamma^\mu \partial_\mu \psi_j(x). \quad (2.8)$$

479 Mass terms are included directly in the QED and QCD free Lagrangians since they
 480 preserve the invariance under the symmetry transformations involved which treat
 481 left-handed and right-handed similarly, however mass terms of the form

$$m_W^2 W_\mu^\dagger(x) W^\mu(x) + \frac{1}{2} m_Z^2 Z_\mu(x) Z^\mu(x) - m_e \bar{\psi}_e(x) \psi_e(x) \quad (2.9)$$

482 which represent the mass of W^\pm , Z and electrons, are not invariant under G trans-
 483 formations, therefore the gauge fields described by the EWI are in principle massless.

484

485 Experiments have shown that the gauge fields are not massless; however, they have

486 to acquire mass through a mechanism compatible with the gauge invariance; that
 487 mechanism is known as the “Higgs mechanism” and will be considered later in this
 488 section. The global transformations in the combined symmetry group G can be
 489 written as

$$\begin{aligned}\psi_1(x) &\xrightarrow{G} \psi'_1(x) \equiv U_Y U_L \psi_1(x), \\ \psi_2(x) &\xrightarrow{G} \psi'_2(x) \equiv U_Y \psi_2(x), \\ \psi_3(x) &\xrightarrow{G} \psi'_3(x) \equiv U_Y \psi_3(x)\end{aligned}\tag{2.10}$$

490 where U_L represent the $SU(2)_L$ transformation acting only on the weak isospin dou-
 491 blet and U_Y represent the $U(1)_Y$ transformation acting on all the weak isospin mul-
 492 tiplets. Explicitly

$$U_L \equiv \exp\left(i\frac{\sigma_i}{2}\alpha^i\right), \quad U_Y \equiv \exp(iy_i\beta) \quad (i = 1, 2, 3)\tag{2.11}$$

493 with σ_i the Pauli matrices and y_i the weak hypercharges. In order to promote the
 494 transformations from global to local while keeping the invariance, it is required that
 495 $\alpha^i = \alpha^i(x)$, $\beta = \beta(x)$ and the replacement of the ordinary derivatives by the covariant
 496 derivatives

$$\begin{aligned}D_\mu \psi_1(x) &\equiv [\partial_\mu + ig\sigma_i W_\mu^i(x)/2 + ig'y_1 B_\mu(x)] \psi_1(x) \\ D_\mu \psi_2(x) &\equiv [\partial_\mu + ig'y_2 B_\mu(x)] \psi_2(x) \\ D_\mu \psi_3(x) &\equiv [\partial_\mu + ig'y_3 B_\mu(x)] \psi_3(x)\end{aligned}\tag{2.12}$$

497 introducing in this way four gauge fields, $W_\mu^i(x)$ and $B_\mu(x)$, in the process. The
 498 covariant derivatives (eqn 2.12) are required to transform in the same way as fermion
 499 fields $\psi_i(x)$ themselves, therefore, the gauge fields transform as:

$$\begin{aligned} B_\mu(x) &\xrightarrow{G} B'_\mu(x) \equiv B_\mu(x) - \frac{1}{g'} \partial_\mu \beta(x) \\ W_\mu^i(x) &\xrightarrow{G} W_\mu^{i\prime}(x) \equiv W_\mu^i(x) - \frac{i}{g} \partial_\mu \alpha_i(x) - \varepsilon_{ijk} \alpha_i(x) W_\mu^j(x). \end{aligned} \quad (2.13)$$

500 The G invariant version of the Lagrangian density 2.8 can be written as

$$\mathcal{L}_0 = \sum_{j=1}^3 i \bar{\psi}_j(x) \gamma^\mu D_\mu \psi_j(x) \quad (2.14)$$

501 where free massless fermion and gauge fields and fermion-gauge boson interactions
 502 are included. The EWI Lagrangian density must additionally include kinetic terms
 503 for the gauge fields (\mathcal{L}_G) which are built from the field strengths, according to

$$B_{\mu\nu}(x) \equiv \partial_\mu B_\nu - \partial_\nu B_\mu \quad (2.15)$$

$$W_{\mu\nu}^i(x) \equiv \partial_\mu W_\nu^i(x) - \partial_\nu W_\mu^i(x) - g \varepsilon^{ijk} W_\mu^j W_\nu^k \quad (2.16)$$

504 the last term in eqn. 2.16 is added in order to hold the gauge invariance; therefore,

$$\mathcal{L}_G = -\frac{1}{4} B_{\mu\nu}(x) B^{\mu\nu}(x) - \frac{1}{4} W_{\mu\nu}^i(x) W_i^{\mu\nu}(x) \quad (2.17)$$

505 which contains not only the free gauge fields contributions, but also the gauge fields
 506 self-interactions and interactions among them.

508 The three weak isospin conserved currents resulting from the $SU(2)_L$ symmetry are
 509 given by

$$J_\mu^i(x) = \frac{1}{2} \bar{\psi}_1(x) \gamma_\mu \sigma^i \psi_1(x) \quad (2.18)$$

510 while the weak hypercharge conserved current resulting from the $U(1)_Y$ symmetry is
 511 given by

$$J_\mu^Y = \sum_{j=1}^3 \bar{\psi}_j(x) \gamma_\mu y_j \psi_j(x) \quad (2.19)$$

512 In order to evaluate the electroweak interactions modeled by an isovector field W_μ^i
 513 which couples to isospin currents J_μ^i with strength g and additionally the singlet
 514 field B_μ which couples to the weak hypercharge current J_μ^Y with strength $g'/2$. The
 515 interaction Lagrangian density to be considered is

$$\mathcal{L}_I = -g J^{i\mu}(x) W_\mu^i(x) - \frac{g'}{2} J^{Y\mu}(x) B_\mu(x) \quad (2.20)$$

516 Note that the weak isospin currents are not the same as the charged fermionic currents
 517 that were used to describe the WI (eqn 2.7), since the weak isospin eigenstates are
 518 not the same as the mass eigenstates, but they are closely related

$$J_\mu = \frac{1}{2} (J_\mu^1 + i J_\mu^2), \quad J_\mu^\dagger = \frac{1}{2} (J_\mu^1 - i J_\mu^2). \quad (2.21)$$

519 The same happens with the gauge fields W_μ^i which are related to the mass eigenstates
 520 W^\pm by

$$W_\mu^+ = \frac{1}{\sqrt{2}} (W_\mu^1 - i W_\mu^2), \quad W_\mu^- = \frac{1}{\sqrt{2}} (W_\mu^1 + i W_\mu^2). \quad (2.22)$$

521 The fact that there are three weak isospin conserved currents is an indication that in
 522 addition to the charged fermionic currents, which couple charged to neutral leptons,
 523 there should be a neutral fermionic current that does not involve electric charge
 524 exchange; therefore, it couples neutral fermions or fermions of the same electric charge.
 525 The third weak isospin current contains a term that is similar to the electromagnetic
 526 current (j_μ^{em}), indicating that there is a relation between them and resembling the
 527 Gell-Mann-Nishijima formula 2.2 adapted to electroweak interactions

$$Q = T_3 + \frac{Y_W}{2}. \quad (2.23)$$

528 Just as Q generates the $U(1)_{em}$ symmetry, the weak hypercharge generates the $U(1)_Y$
 529 symmetry as said before. It is possible to write the relationship in terms of the currents
 530 as

$$j_\mu^{em} = J_\mu^3 + \frac{1}{2}J_\mu^Y. \quad (2.24)$$

531 The neutral gauge fields W_μ^3 and B_μ cannot be directly identified with the Z and the
 532 photon fields since the photon interacts similarly with left and right-handed fermions;
 533 however, they are related through a linear combination given by

$$\begin{aligned} A_\mu &= B_\mu \cos \theta_W + W_\mu^3 \sin \theta_W \\ Z_\mu &= -B_\mu \sin \theta_W + W_\mu^3 \cos \theta_W \end{aligned} \quad (2.25)$$

534 where θ_W is known as the “Weinberg angle.” The interaction Lagrangian is now given

535 by

$$\mathcal{L}_I = -\frac{g}{\sqrt{2}}(J^\mu W_\mu^+ + J^{\mu\dagger} W_\mu^-) - \left(g \sin \theta_W J_\mu^3 + g' \cos \theta_W \frac{J_\mu^Y}{2}\right) A^\mu - \left(g \cos \theta_W J_\mu^3 - g' \sin \theta_W \frac{J_\mu^Y}{2}\right) Z^\mu \quad (2.26)$$

536 the first term is the weak charged current interaction, while the second term is the
537 electromagnetic interaction under the condition

$$g \sin \theta_W = g' \cos \theta_W = e, \quad \frac{g'}{g} = \tan \theta_W \quad (2.27)$$

538 contained in the eqn.2.24; the third term is the neutral weak current.

539

540 Note that the neutral fields transformation given by the eqn. 2.25 can be written in
541 terms of the coupling constants g and g' as:

$$A_\mu = \frac{g' W_\mu^3 + g B_\mu}{\sqrt{g^2 + g'^2}}, \quad Z_\mu = \frac{g W_\mu^3 - g' B_\mu}{\sqrt{g^2 + g'^2}} \quad (2.28)$$

542 So far, the Lagrangian density describing the non-massive EWI is:

$$\mathcal{L}_{nmEWI} = \mathcal{L}_0 + \mathcal{L}_G \quad (2.29)$$

543 where fermion and gauge fields have been considered massless because their regular
544 mass terms are manifestly non invariant under G transformations; therefore, masses
545 have to be generated in a gauge invariant way. The mechanism by which this goal is
546 achieved is known as the “Higgs mechanism” and is closely connected to the concept
547 of “spontaneous symmetry breaking.”

548 **2.3.1 Spontaneous symmetry breaking (SSB)**

549 Figure 2.6 left shows a steel nail (top) which is subject to an external force; the form
 550 of the potential energy is also shown (bottom).

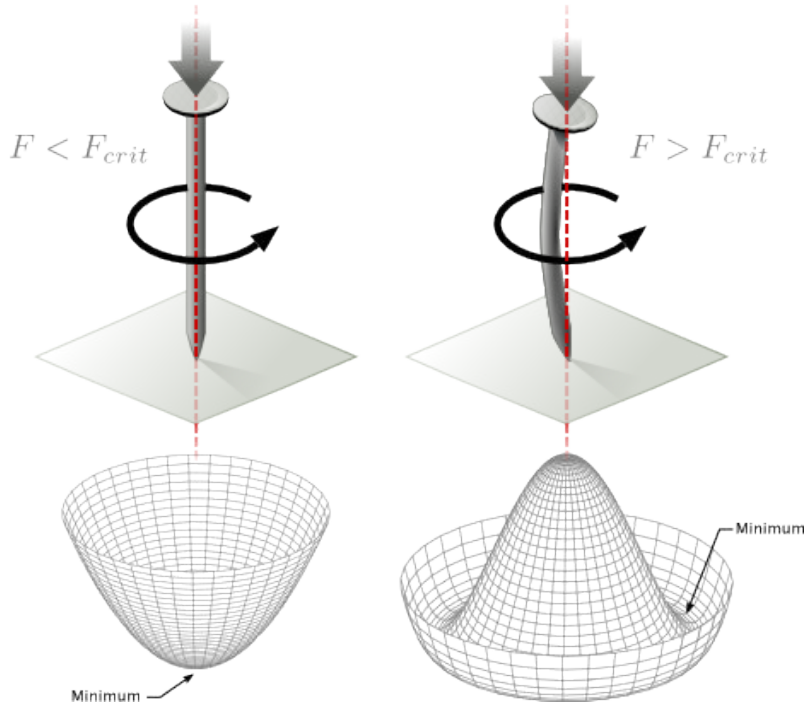


Figure 2.6: Spontaneous symmetry breaking mechanism. The steel nail, subject to an external force (top left), has rotational symmetry with respect to its axis. When the external force overcomes a critical value the nail buckles (top right) choosing a minimal energy state (ground state) and thus “*breaking spontaneously the rotational symmetry*”. The potential energy (bottom) changes but holds the rotational symmetry; however, an infinite number of asymmetric ground states are generated and circularly distributed in the bottom of the potential [27].

551

552 Before reaching the critical force value, the system has rotational symmetry with re-
 553 spect to the nail axis; however, after the critical force value is reached the nail buckles
 554 (top right). The form of the potential energy (bottom right) changes, preserving its
 555 rotational symmetry although its minima does not exhibit that rotational symmetry
 556 any longer. Right before the nail buckles there is no indication of the direction the

557 nail will bend because any of the directions are equivalent, but once the nail bends,
 558 choosing a direction, an arbitrary minimal energy state (ground state) is selected and
 559 it does not share the system's rotational symmetry. This mechanism for reaching an
 560 asymmetric ground state is known as "*spontaneous symmetry breaking*".

561 The lesson from this analysis is that the way to introduce the SSB mechanism into a
 562 system is by adding the appropriate potential to it.

563

564 Figure 2.7 shows a plot of the potential $V(\phi)$ in the case of a scalar field ϕ

$$V(\phi) = \mu^2 \phi^\dagger \phi + \lambda (\phi^\dagger \phi)^2 \quad (2.30)$$

565 If $\mu^2 > 0$ the potential has only one minimum at $\phi = 0$ and describes a scalar field
 566 with mass μ . If $\mu^2 < 0$ the potential has a local maximum at $\phi = 0$ and two minima
 567 at $\phi = \pm\sqrt{-\mu^2/\lambda}$ which enables the SSB mechanism to work.

568

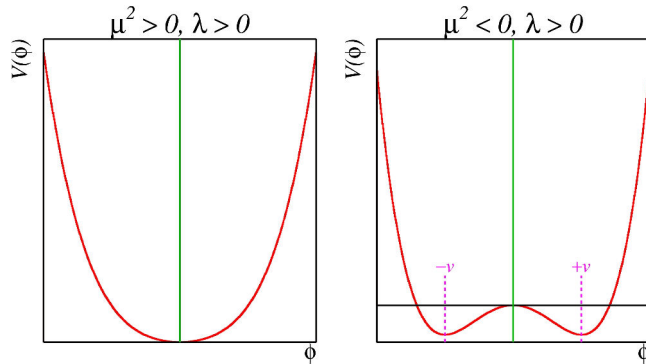


Figure 2.7: Shape of the potential $V(\phi)$ for $\lambda > 0$ and: $\mu^2 > 0$ (left) and $\mu^2 < 0$ (right). The case $\mu^2 < 0$ corresponds to the potential suitable for introducing the SSB mechanism by choosing one of the two ground states which are connected via reflection symmetry. [27].

569 In the case of a complex scalar field $\phi(x)$

$$\phi(x) = \frac{1}{\sqrt{2}}(\phi_1 + i\phi_2) \quad (2.31)$$

570 the Lagrangian (invariant under global $U(1)$ transformations) is given by

$$\mathcal{L} = (\partial_\mu \phi)^\dagger (\partial^\mu \phi) - V(\phi), \quad V(\phi) = \mu^2 \phi^\dagger \phi + \lambda (\phi^\dagger \phi)^2 \quad (2.32)$$

571 where an appropriate potential has been added in order to introduce the SSB.

572

573 As seen in figure 2.8, the potential has now an infinite number of minima circularly
 574 distributed along the ξ -direction which makes possible the occurrence of the SSB by
 575 choosing an arbitrary ground state; for instance, $\xi = 0$, i.e. $\phi_1 = v, \phi_2 = 0$

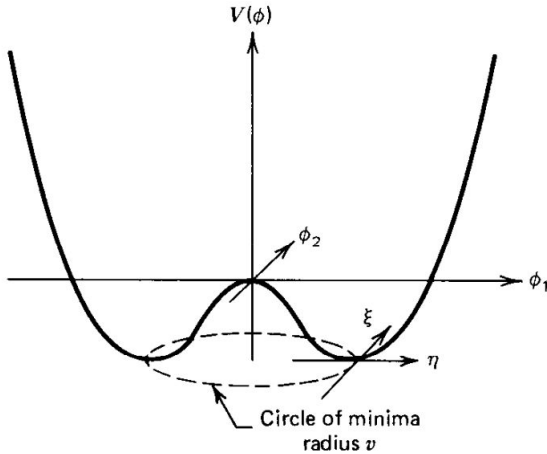


Figure 2.8: Potential for complex scalar field. There is a circle of minima of radius v along the ξ -direction [6].

$$\phi_0 = \frac{v}{\sqrt{2}} \exp(i\xi) \xrightarrow{SSB} \phi_0 = \frac{v}{\sqrt{2}} \quad (2.33)$$

576 As usual, excitations over the ground state are studied by making an expansion about

577 it; thus, the excitation can be parametrized as:

$$\phi(x) = \frac{1}{\sqrt{2}}(v + \eta(x) + i\xi(x)) \quad (2.34)$$

578 which when substituted into eqn. 2.32 produces a Lagrangian in terms of the new
 579 fields η and ξ

$$\mathcal{L}' = \frac{1}{2}(\partial_\mu\xi)^2 + \frac{1}{2}(\partial_\mu\eta)^2 + \mu^2\eta^2 - V(\phi_0) - \lambda v\eta(\eta^2 + \xi^2) - \frac{\lambda}{4}(\eta^2 + \xi^2)^2 \quad (2.35)$$

580 where the last two terms represent the interactions and self-interaction between the
 581 two fields η and ξ . The particular feature of the SSB mechanism is revealed when
 582 looking to the first three terms of \mathcal{L}' . Before the SSB, only the massless ϕ field is
 583 present in the system; after the SSB there are two fields of which the η -field has
 584 acquired mass $m_\eta = \sqrt{-2\mu^2}$ while the ξ -field is still massless (see figure 2.9).

585

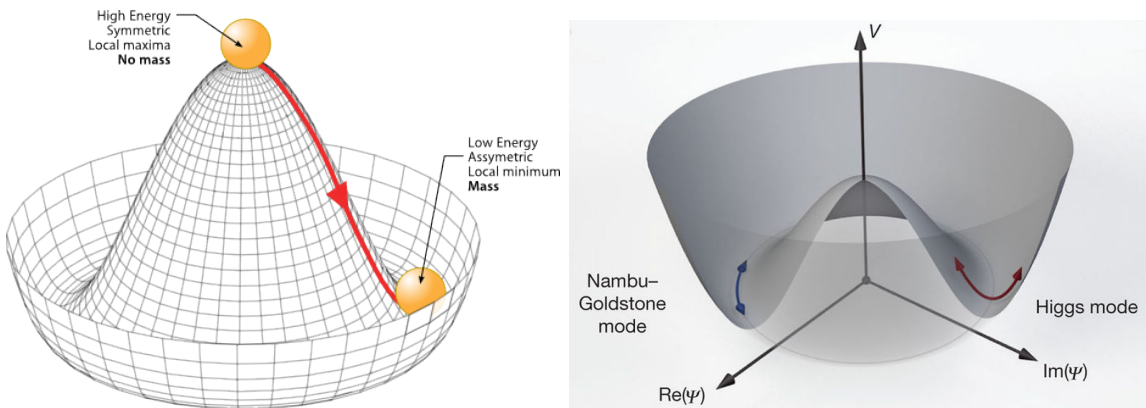


Figure 2.9: SSB mechanism for a complex scalar field [27, 28].

586 Thus, the SSB mechanism serves as a method to generate mass but as a side effect a
 587 massless field is introduced in the system. This fact is known as the Goldstone theorem

and states that a massless scalar field appears in the system for each continuous symmetry spontaneously broken. Another version of the Goldstone theorem states that “*if a Lagrangian is invariant under a continuous symmetry group G , but the vacuum is only invariant under a subgroup $H \subset G$, then there must exist as many massless spin-0 particles (Nambu-Goldstone bosons) as broken generators.*” [26] The Nambu-Goldstone boson can be understood considering that the potential in the ξ -direction is flat so excitations in that direction are not energy consuming and thus represent a massless state.

2.3.2 Higgs mechanism

When the SSB mechanism is introduced in the formulation of the EWI in an attempt to generate the mass of the so far massless gauge bosons and fermions, an interesting effect is revealed. In order to keep the G symmetry group invariance and generate the mass of the EW gauge bosons, a G invariant Lagrangian density (\mathcal{L}_S) has to be added to the non massive EWI Lagrangian (eqn. 2.29)

$$\mathcal{L}_S = (D_\mu \phi)^\dagger (D^\mu \phi) - \mu^2 \phi^\dagger \phi - \lambda (\phi^\dagger \phi)^2, \quad \lambda > 0, \mu^2 < 0 \quad (2.36)$$

$$D_\mu \phi = \left(i\partial_\mu - g \frac{\sigma_i}{2} W_\mu^i - g' \frac{Y}{2} B_\mu \right) \phi \quad (2.37)$$

ϕ has to be an isospin doublet of complex scalar fields so it preserves the G invariance; thus ϕ can be defined as:

$$\phi = \begin{pmatrix} \phi^+ \\ \phi^0 \end{pmatrix} \equiv \frac{1}{\sqrt{2}} \begin{pmatrix} \phi_1 + i\phi_2 \\ \phi_3 + i\phi_4 \end{pmatrix}. \quad (2.38)$$

The minima of the potential are defined by

$$\phi^\dagger \phi = \frac{1}{2}(\phi_1^2 + \phi_2^2 + \phi_3^2 + \phi_4^2) = -\frac{\mu^2}{2\lambda}. \quad (2.39)$$

605 The choice of the ground state is critical. By choosing a ground state, invariant under
 606 $U(1)_{em}$ gauge symmetry, the photon will remain massless and the W^\pm and Z bosons
 607 masses will be generated which is exactly what is needed. In that sense, the best
 608 choice corresponds to a weak isospin doublet with $T_3 = -1/2$, $Y_W = 1$ and $Q = 0$
 609 which defines a ground state with $\phi_1 = \phi_2 = \phi_4$ and $\phi_3 = v$:

$$\phi_0 \equiv \frac{1}{\sqrt{2}} \begin{pmatrix} 0 \\ v \end{pmatrix}, \quad v^2 \equiv -\frac{\mu^2}{\lambda}. \quad (2.40)$$

610 where the vacuum expectation value v is fixed by the Fermi coupling G_F according
 611 to $v = (\sqrt{2}G_F)^{1/2} \approx 246$ GeV.

612

613 The G symmetry has been broken and three Nambu-Goldstone bosons will appear.
 614 The next step is to expand ϕ about the chosen ground state as:

$$\phi(x) = \frac{1}{\sqrt{2}} \exp\left(\frac{i}{v} \sigma_i \theta^i(x)\right) \begin{pmatrix} 0 \\ v + H(x) \end{pmatrix} \approx \frac{1}{\sqrt{2}} \begin{pmatrix} \theta_1(x) + i\theta_2(x) \\ v + H(x) - i\theta_3(x) \end{pmatrix} \quad (2.41)$$

615 to describe fluctuations from the ground state ϕ_0 . The fields $\theta_i(x)$ represent the
 616 Nambu-Goldstone bosons while $H(x)$ is known as “higgs field.” The fundamental
 617 feature of the parametrization used is that the dependence on the $\theta_i(x)$ fields is
 618 factored out in a global phase that can be eliminated by taking the physical “unitary
 619 gauge” $\theta_i(x) = 0$. Therefore the expansion about the ground state is given by:

$$\phi(x) \frac{1}{\sqrt{2}} \begin{pmatrix} 0 \\ v + H(x) \end{pmatrix} \quad (2.42)$$

620 which when substituted into \mathcal{L}_S (eqn. 2.36) results in a Lagrangian containing the now
 621 massive three gauge bosons W^\pm, Z , one massless gauge boson (photon) and the new
 622 Higgs field (H). The three degrees of freedom corresponding to the Nambu-Goldstone
 623 bosons are now integrated into the massive gauge bosons as their longitudinal po-
 624 larizations which were not available when they were massless particles. The effect
 625 by which vector boson fields acquire mass after an spontaneous symmetry breaking,
 626 but without an explicit gauge invariance breaking is known as the “*Higgs mechanism*”.

627

628 The mechanism was proposed by three independent groups: F.Englert and R.Brout
 629 in August 1964 [29], P.Higgs in October 1964 [30] and G.Guralnik, C.Hagen and
 630 T.Kibble in November 1964 [31]; however, its importance was not realized until
 631 S.Glashow [22], A.Salam [23] and S.Weinberg [24], independently, proposed that elec-
 632 tromagnetic and weak interactions are two manifestations of a more general interac-
 633 tion called “electroweak interaction” in 1967.

634 2.3.3 Masses of the gauge bosons

635 The mass of the gauge bosons is extracted by evaluating the kinetic part of Lagrangian
 636 \mathcal{L}_S in the ground state (known also as the vacuum expectation value), i.e.,

$$\left| \left(\partial_\mu - ig \frac{\sigma_i}{2} W_\mu^i - i \frac{g'}{2} B_\mu \right) \phi_0 \right|^2 = \left(\frac{1}{2} v g \right)^2 W_\mu^+ W^{-\mu} + \frac{1}{8} v^2 (W_\mu^3, B_\mu) \begin{pmatrix} g^2 & -gg' \\ -gg' & g'^2 \end{pmatrix} \begin{pmatrix} W^{3\mu} \\ B^\mu \end{pmatrix} \quad (2.43)$$

637 comparing with the typical mass term for a charged boson $M_W^2 W^+ W^-$

$$M_W = \frac{1}{2} v g. \quad (2.44)$$

The second term in the right side of the eqn.2.43 comprises the masses of the neutral

bosons, but it needs to be written in terms of the gauge fields Z_μ and A_μ in order to be compared to the typical mass terms for neutral bosons, therefore using eqn. 2.28

$$\begin{aligned} \frac{1}{8}v^2[g^2(W_\mu^3)^2 - 2gg'W_\mu^3B^\mu + g'^2B_\mu^2] &= \frac{1}{8}v^2[gW_\mu^3 - g'B_\mu]^2 + 0[g'W_\mu^3 + gB_\mu]^2 \\ &= \frac{1}{8}v^2[\sqrt{g^2 + g'^2}Z_\mu]^2 + 0[\sqrt{g^2 + g'^2}A_\mu]^2 \end{aligned} \quad (2.45)$$

638 and then

$$M_Z = \frac{1}{2}v\sqrt{g^2 + g'^2}, \quad M_A = 0 \quad (2.46)$$

639 2.3.4 Masses of the fermions

640 The lepton mass terms can be generated by introducing a gauge invariant Lagrangian
641 term describing the Yukawa coupling between the lepton field and the Higgs field

$$\mathcal{L}_{Yl} = -G_l \left[(\bar{\nu}_l, \bar{l})_L \begin{pmatrix} \phi^+ \\ \phi^0 \end{pmatrix} l_R + \bar{l}_R (\phi^-, \bar{\phi}^0) \begin{pmatrix} \nu_l \\ l \end{pmatrix}_L \right], \quad l = e, \mu, \tau. \quad (2.47)$$

642 After the SSB and replacing the usual field expansion about the ground state (eqn.2.40)
643 into \mathcal{L}_{Yl} , the mass term arises

$$\mathcal{L}_{Yl} = -m_l(\bar{l}_L l_R + \bar{l}_R l_L) - \frac{m_l}{v}(\bar{l}_L l_R + \bar{l}_R l_L)H = -m_l \bar{l} \left(1 + \frac{H}{v} \right) \quad (2.48)$$

644

$$m_l = \frac{G_l}{\sqrt{2}}v \quad (2.49)$$

645 where the additional term represents the lepton-Higgs interaction. The quark masses
646 are generated in a similar way as lepton masses but for the upper member of the

647 quark doublet a different Higgs doublet is needed:

$$\phi_c = -i\sigma_2\phi^* = \begin{pmatrix} -\bar{\phi}^0 \\ \phi^- \end{pmatrix}. \quad (2.50)$$

648 Additionally, given that the quark isospin doublets are not constructed in terms of
 649 the mass eigenstates but in terms of the flavor eigenstates, as shown in table 2.5, the
 650 coupling parameters will be related to the CKM matrix elements; thus the quark
 651 Lagrangian is given by:

$$\mathcal{L}_{Yq} = -G_d^{i,j}(\bar{u}_i, \bar{d}_i)_L \begin{pmatrix} \phi^+ \\ \phi^0 \end{pmatrix} d_{jR} - G_u^{i,j}(\bar{u}_i, \bar{d}_i)_L \begin{pmatrix} -\bar{\phi}^0 \\ \phi^- \end{pmatrix} u_{jR} + h.c. \quad (2.51)$$

652 with $i,j=1,2,3$. After SSB and expansion about the ground state, the diagonal form
 653 of \mathcal{L}_{Yq} is:

$$\mathcal{L}_{Yq} = -m_d^i \bar{d}_i d_i \left(1 + \frac{H}{v} \right) - m_u^i \bar{u}_i u_i \left(1 + \frac{H}{v} \right) \quad (2.52)$$

654 Fermion masses depend on arbitrary couplings G_l and $G_{u,d}$ and are not predicted by
 655 the theory.

656 2.3.5 The Higgs field

657 After the characterization of the fermions and gauge bosons as well as their interac-
 658 tions, it is necessary to characterize the Higgs field itself. The Lagrangian \mathcal{L}_S in eqn.
 659 2.3.6 written in terms of the gauge bosons is given by

$$\mathcal{L}_S = \frac{1}{4}\lambda v^4 + \mathcal{L}_H + \mathcal{L}_{HV} \quad (2.53)$$

660

$$\mathcal{L}_H = \frac{1}{2}\partial_\mu H \partial^\mu H - \frac{1}{2}m_H^2 H^2 - \frac{1}{2v}m_H^2 H^3 - \frac{1}{8v^2}m_H^2 H^4 \quad (2.54)$$

661

$$\mathcal{L}_{HV} = m_H^2 W_\mu^+ W^{\mu-} \left(1 + \frac{2}{v}H + \frac{2}{v^2}H^2 \right) + \frac{1}{2}m_Z^2 Z_\mu Z^\mu \left(1 + \frac{2}{v}H + \frac{2}{v^2}H^2 \right) \quad (2.55)$$

662 The mass of the Higgs boson is deduced as usual from the mass term in the Lagrangian
 663 resulting in:

$$m_H = \sqrt{-2\mu^2} = \sqrt{2\lambda}v \quad (2.56)$$

664 however, it is not predicted by the theory either. The experimental efforts to find
 665 the Higgs boson, carried out by the “Compact Muon Solenoid (CMS)” experiment
 666 and the “A Toroidal LHC AppartuS (ATLAS)” experiments at the “Large Hadron
 667 Collider(LHC)”, gave great results by July of 2012 when the discovery of a new
 668 particle compatible with the Higgs boson predicted by the electroweak theory [32,33]
 669 was announced. Although at the announcement time there were some reservations
 670 about calling the new particle the “Higgs boson”, today this name is widely accepted.
 671 The Higgs mass measurement, reported by both experiments [34], is in table 2.8.

Property	Value
Electric charge	0
Colour charge	0
Spin	0
Weak isospin	-1/2
Weak hypercharge	1
Parity	1
Mass (GeV/c ²)	125.09±0.21 (stat.)±0.11 (syst.)

Table 2.8: Higgs boson properties. Higgs mass is not predicted by the theory and the value here corresponds to the experimental measurement.

672

673 2.3.6 Production of Higgs bosons at LHC

674 At LHC, Higgs boson is produced as a result of the collision of two counter-rotating
 675 protons beams. A detailed description of the LHC machine will be presented in
 676 chapter 3. “The total cross section” is a parameter that quantifies the number of pp
 677 collisions that happen when a number of protons are fired at each other. Different
 678 results can be obtained after a pp collision and for each one the “cross section” is

679 defined as the number of pp collisions that conclude in that particular result with
 respect to the number of protons fired at each other.

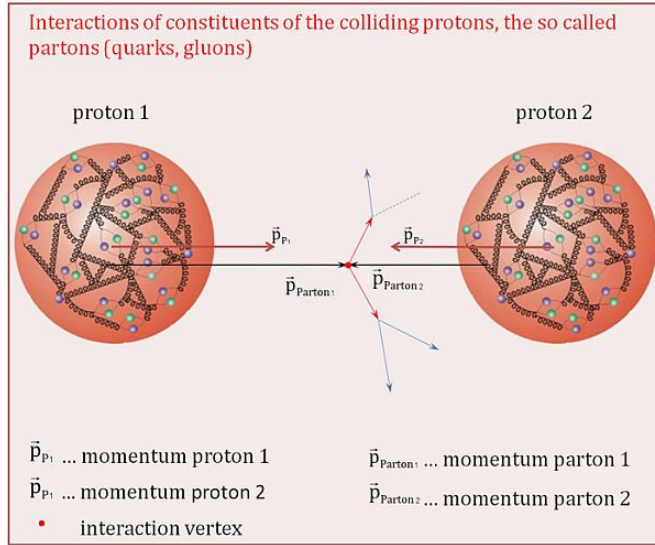


Figure 2.10: Proton-proton collision. Protons are composed of 3 valence quarks, a sea of quarks and gluons; therefore in a proton-proton collision, quarks and gluons are those who collide. [35].

680

681 Protons are composed of quarks and these quarks are bound by gluons; however,
 682 what is commonly called the quark content of the proton makes reference to the
 683 valence quarks. A sea of quarks and gluons is also present inside the proton as repre-
 684 sented in figure 2.10. In a proton-proton (pp) collision, the constituents (quarks and
 685 gluons) are those who collide. The pp cross section depends on the momentum of
 686 the colliding particles, reason for which it is needed to know how the momentum is
 687 distributed inside the proton. Quarks and gluons are known as partons and the func-
 688 tions that describe how the proton momentum is distributed among partons inside it
 689 are called “parton distribution functions (PDFs)”; PDFs are determined from experi-
 690 mental data obtained in experiments where the internal structure of hadrons is tested.

691

692 In addition, in physics, a common approach to study complex systems consists in

693 starting with a simpler version of them, for which a well known description is avail-
 694 able, and add an additional “perturbation” which represents a small deviation from
 695 the known behavior. If the perturbation is small enough, the physical quantities as-
 696 sociated with the perturbed system are expressed as a series of corrections to those
 697 of the simpler system; therefore, the more terms are considered in the series (the
 698 higher order in the perturbation series), the more precise is the the description of the
 699 complex system.

700

701 This thesis explores the Higgs production at LHC; therefore the overview presented
 702 here will be oriented specifically to the production mechanisms after pp collisions at
 703 LHC.

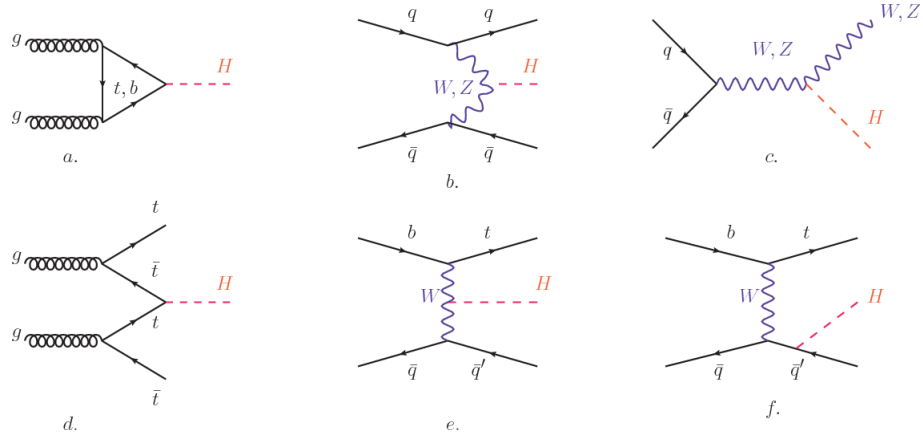


Figure 2.11: Main Higgs boson production mechanism Feynman diagrams. a. gluon-gluon fusion, b. vector boson fusion (VBF), c. Higgs-strahlung, d. Associated production with a top or bottom quark pair, e-f. associated production with a single top quark.

704 Figure 2.11 shows the Feynman diagrams for the leading order (first order) Higgs
 705 production processes at LHC, while the cross section for Higgs production as a func-
 706 tion of the center of mass-energy (\sqrt{s}) for pp collisions is showed in figure 2.12 left.
 707 The tags NLO (next to leading order), NNLO (next to next to leading order) and
 708 N3LO (next to next to next to leading order) make reference to the order at which

the perturbation series have been considered.

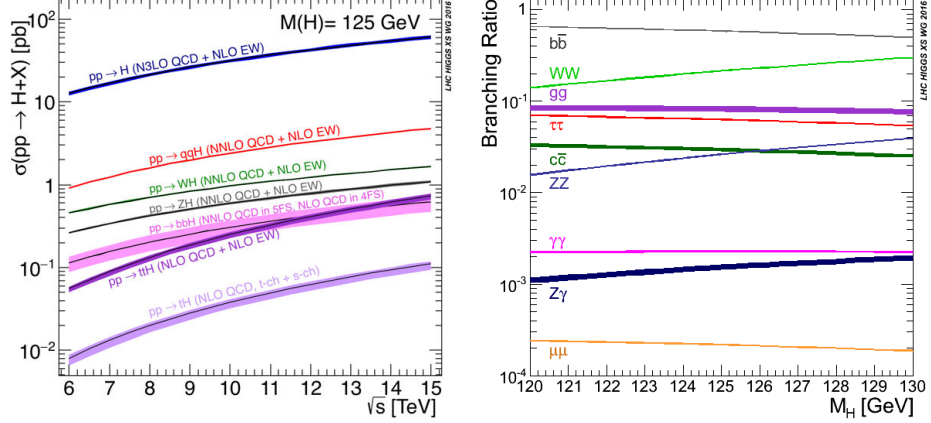


Figure 2.12: Higgs boson production cross sections (left) and decay branching ratios (right) for the main mechanisms. The VBF is indicated as $q\bar{q}H$ [36].

As shown in eqns 2.47, 2.51 and 2.55, the strength of the Higgs-fermion interaction is proportional to the fermion mass while the strength of the Higgs-gauge boson interaction is proportional to the square of the gauge boson mass, which implies that the Higgs production and decay mechanisms are dominated by couplings $H - (W, Z, t, b, \tau)$.

The main production mechanism is the gluon fusion (figure 2.11a and $pp \rightarrow H$ in figure 2.12) given that gluons carry the highest fraction of momentum of the protons in pp colliders. Since the Higgs boson does not couple to gluons, the mechanism proceeds through the exchange of a virtual top-quark loop given that for it the coupling is the biggest. Note that in this process, the Higgs boson is produced alone, which makes this mechanism experimentally clean when combined with the two-photon or the four-lepton decay channels (see section 2.3.7).

Vector boson fusion (figure 2.11b and $pp \rightarrow q\bar{q}H$ in figure 2.12) has the second largest production cross section. The scattering of two fermions is mediated by a weak gauge boson which later emits a Higgs boson. In the final state, the two fermions

725 tend to be located in a particular region of the detector which is used as a signature
 726 when analyzing the datasets provided by the experiments. More details about how
 727 to identify events of interest in an analysis will be given in chapter ??.

728 The next production mechanism is Higgs-strahlung (figure 2.11c and $pp \rightarrow WH, pp \rightarrow$
 729 ZH in figure 2.12) where two fermions annihilate to form a weak gauge boson. If the
 730 initial fermions have enough energy, the emergent boson eventually will emit a Higgs
 731 boson.

732 The associated production with a top or bottom quark pair and the associated pro-
 733 duction with a single top quark (figure 2.11d-f and $pp \rightarrow bbH, pp \rightarrow t\bar{t}H, pp \rightarrow tH$
 734 in figure 2.12) have a smaller cross section than the main three mechanisms above,
 735 but they provide a good opportunity to test the Higgs-top coupling. The analysis
 736 reported in this thesis is developed using these production mechanisms. A detailed
 737 description of the tH mechanism will be given in section 2.4.

738 2.3.7 Higgs boson decay channels

739 When a particle can decay through several modes, also known as channels, the
 740 probability of decaying through a given channel is quantified by the “branching ratio
 741 (BR)” of the decay channel; thus, the BR is defined as the ratio of number of decays
 742 going through that given channel to the total number of decays. In regard to the
 743 Higgs boson decay, the BR can be predicted with accuracy once the Higgs mass is
 744 known [37, 38]. In figure 2.12 right, a plot of the BR as a function of the Higgs mass
 745 is presented. The largest predicted BR corresponds to the $b\bar{b}$ pair decay channel (see
 746 table 2.9).

Decay channel	Branching ratio	Rel. uncertainty
$H \rightarrow bb$	5.84×10^{-1}	+3.2% – 3.3%
$H \rightarrow W^+W^-$	2.14×10^{-1}	+4.3% – 4.2%
$H \rightarrow \tau^+\tau^-$	6.27×10^{-2}	+5.7% – 5.7%
$H \rightarrow ZZ$	2.62×10^{-2}	+4.3% – 4.1%
$H \rightarrow \gamma\gamma$	2.27×10^{-3}	+5.0% – 4.9%
$H \rightarrow Z\gamma$	1.53×10^{-3}	+9.0% – 8.9%
$H \rightarrow \mu^+\mu^-$	2.18×10^{-4}	+6.0% – 5.9%

Table 2.9: Predicted branching ratios and the relative uncertainty for a SM Higgs boson with $m_H = 125 GeV/c^2$. [9]

748 2.4 Associated production of a Higgs boson and a 749 single Top quark.

750 Associated production of Higgs boson has been extensively studied [39–43]. While
751 measurements of the main Higgs production mechanisms rates are sensitive to the
752 strength of the Higgs coupling to W boson or top quark, they are not sensitive to the
753 relative sign between the two couplings. In this thesis, the Higgs boson production
754 mechanism explored is the associated production with a single top quark (*th*) which
755 offers sensitiveness to the relative sign of the Higgs couplings to W boson and to top
756 quark. The description given here is based on the reference [41]

757
758 A process where two incoming particles interact and produce a final state with two
759 particles can proceed in three ways also called channels (see, for instance, figure 2.13
760 ommiting the red line). The t-channel represents processes where an intermediate
761 particle is emitted by one of the incoming particles and absorbed by the other. The
762 s-channel represents processes where the two incoming particles merge into an inter-
763 mediate particle which eventually will split into the particles in the final state. The
764 third channel, u-channel, is similar to the t-channel but the two outgoing particles

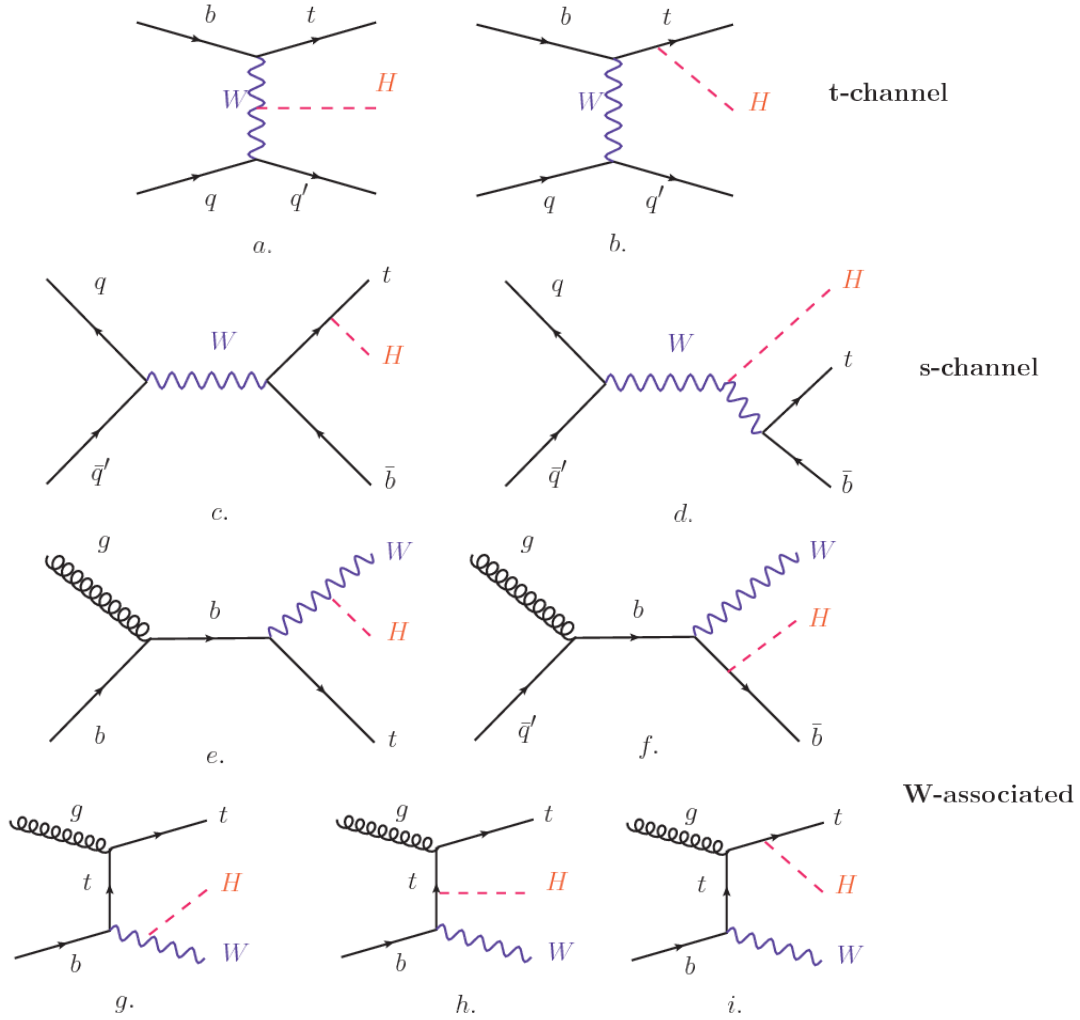


Figure 2.13: Associated Higgs boson production mechanism Feynman diagrams. a.,b. t-channel (tHq), c.,d. s-channel (tHb), e-i. W-associated.

765 interchange their roles.

766

767 The *th* production, where Higgs boson can be radiated either from the top quark or
 768 from the W boson, is represented by the leading order Feynman diagrams in figure
 769 2.13. The cross section for the *th* process is calculated, as usual, summing over
 770 the contributions from the different feynman diagrams; therefore it depends on the
 771 interference between the contributions. In the SM, the interference for t-channel (tHq

772 process) and W-associated (tHW process) production is destructive [39] resulting in
 773 the small cross sections presented in table 2.10.

tH production channel	Cross section (fb)
t-channel ($pp \rightarrow tHq$)	$70.79^{+2.99}_{-4.80}$
W-associated ($pp \rightarrow tHW$)	$15.61^{+0.83}_{-1.04}$
s-channel($pp \rightarrow tHb$)	$2.87^{+0.09}_{-0.08}$

Table 2.10: Predicted SM cross sections for tH production at $\sqrt{s} = 13$ TeV [44, 45].

774

775 While the s-channel contribution can be neglected, it will be shown that a deviation
 776 from the SM destructive interference would result in an enhancement of the th cross
 777 section compared to that in SM, which could be used to get information about the
 778 sign of the Higgs-top coupling [41, 42]. In order to describe th production processes,
 779 Feynman diagram 2.13b will be considered; there, the W boson is radiated by a
 780 quark in the proton and eventually it will interact with the b quark. In the high
 781 energy regime, the effective W approximation [46] allows to describe the process as
 782 the emmission of an approximately on-shell W and its hard scattering with the b
 783 quark; i.e. $Wb \rightarrow th$. The scattering amplitude for the process is given by

$$\mathcal{A} = \frac{g}{\sqrt{2}} \left[(\kappa_t - \kappa_V) \frac{m_t \sqrt{s}}{m_W v} A \left(\frac{t}{s}, \varphi; \xi_t, \xi_b \right) + \left(\kappa_V \frac{2m_W s}{v} \frac{1}{t} + (2\kappa_t - \kappa_V) \frac{m_t^2}{m_W v} \right) B \left(\frac{t}{s}, \varphi; \xi_t, \xi_b \right) \right], \quad (2.57)$$

784 where $\kappa_V \equiv g_{HVV}/g_{HVV}^{SM}$ and $\kappa_t \equiv g_{Ht}/g_{Ht}^{SM} = y_t/y_t^{SM}$ are scaling factors that quan-
 785 tify possible deviations of the couplings, Higgs-Vector boson (H-W) and Higgs-top
 786 (H-t) respectively, from the SM couplings; $s = (p_W + p_b)^2$, $t = (p_W - p_H)^2$, φ is the
 787 Higgs azimuthal angle around the z axis taken parallel to the direction of motion of
 788 the incoming W; A and B are funtions describing the weak interaction in terms of

789 the chiral states of the quarks b and t . Terms that vanish in the high energy limit
 790 have been neglected as well as the Higgs and b quark masses⁸.

791

792 The scattering amplitude grows with energy like \sqrt{s} for $\kappa_V \neq \kappa_t$, in contrast to
 793 the SM ($\kappa_t = \kappa_V = 1$), where the first term in 2.57 cancels out and the amplitude
 794 is constant for large s ; therefore, a deviation from the SM predictions represents an
 795 enhancement in the tHq cross section. In particular, for a SM H-W coupling and a H-t
 796 coupling of inverted sign with respect to the SM ($\kappa_V = -\kappa_t = 1$) the tHq cross section
 797 is enhanced by a factor greater 10 as seen in the figure 2.14 taken from reference [41];
 798 reference [47] has reported similar enhancement results.

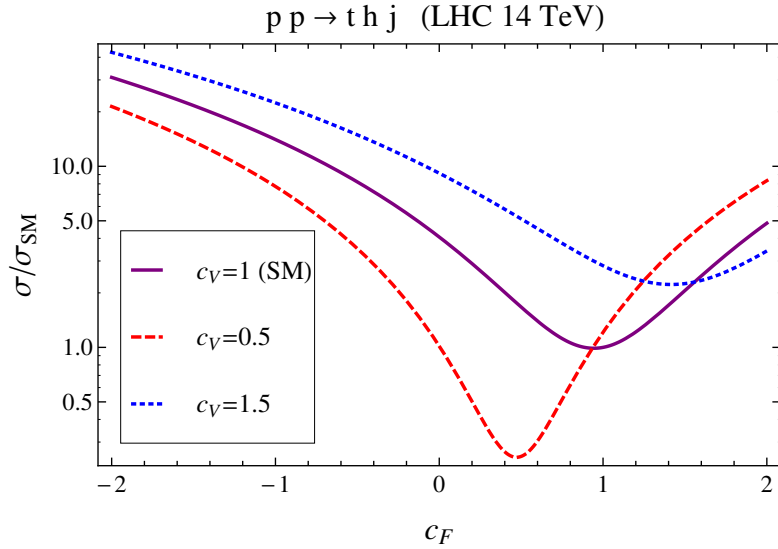


Figure 2.14: Cross section for tHq process as a function of κ_t , normalized to the SM, for three values of κ_V . In the plot c_f refers to the Higgs-fermion coupling which is dominated by the H-t coupling and represented here by κ_t . Solid, dashed and dotted lines correspond to $c_V \rightarrow \kappa_V = 1, 0.5, 1.5$ respectively. Note that for the SM ($\kappa_V = \kappa_t = 1$), the destructive effect of the interference is maximal.

799 A similar analysis is valid for the W-associated channel but, in that case, the inter-
 800 ference is more complicated since there are more than two contributions and an ad-

⁸ A detailed explanation of the structure and approximations used to derive \mathcal{A} can be found in reference [41]

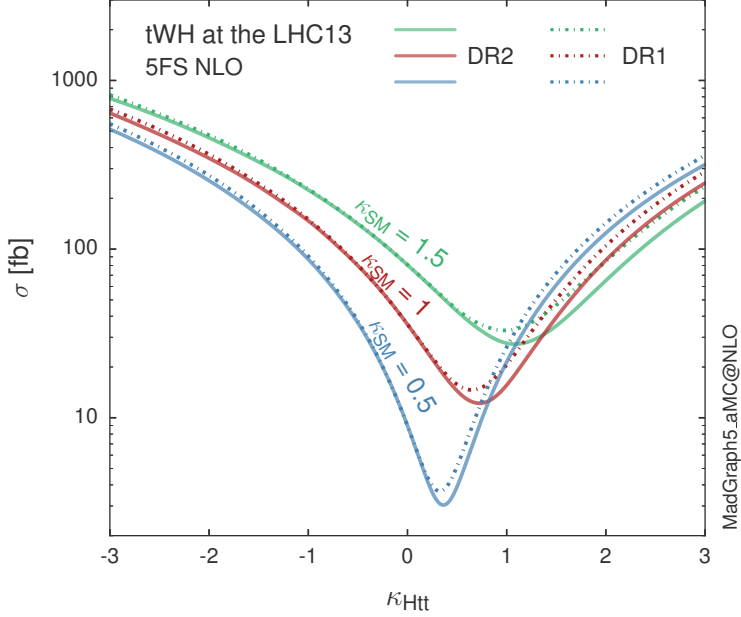


Figure 2.15: Cross section for tHW process as a function of κ_{Htt} , for three values of κ_{SSM} at $\sqrt{s} = 13$ TeV. $\kappa_{Htt}^2 = \sigma_{Htt}/\sigma_{Htt}^{SM}$ is a simple rescaling of the SM Higgs interactions.

ditional interference with the production of Higgs boson and a top pair process($t\bar{t}H$).
 The calculations are made using the so-called Diagram Removal (DR) technique where
 interfering diagrams are removed (or added) from the calculations in order to evaluate
 the impact of the removed contributions. DR1 was defined to neglect $t\bar{t}H$ interference
 while DR2 was defined to take $t\bar{t}H$ interference into account [48]. As shown in figure
 2.15, the tHW cross section is enhanced from about 15 fb (SM: $\kappa_{Htt} = 1$) to about
 150 fb ($\kappa_{Htt} = -1$). Differences between curves for DR1 and DR2 help to gauge the
 impact of the interference with $t\bar{t}H$.
 Results of the calculations of the tHq and tHW cross sections at $\sqrt{s} = 13$ TeV can be
 found in reference [49] and a summary of the results is presented in table 2.11.

	\sqrt{s} TeV	$\kappa_t = 1$	$\kappa_t = -1$
$\sigma^{LO}(tHq)(fb)$ [41]	8	≈ 17.4	≈ 252.7
	14	≈ 80.4	≈ 1042
$\sigma^{NLO}(tHq)(fb)$ [41]	8	$18.28^{+0.42}_{-0.38}$	$233.8^{+4.6}_{-0.0}$
	14	$88.2^{+1.7}_{-0.0}$	$982.8^{+28}_{-0.0}$
$\sigma^{LO}(tHq)(fb)$ [47]	14	≈ 71.8	≈ 893
$\sigma^{LO}(tHW)(fb)$ [47]	14	≈ 16.0	≈ 139
$\sigma^{NLO}(tHq)(fb)$ [49]	8	$18.69^{+8.62\%}_{-17.13\%}$	-
	13	$74.25^{+7.48\%}_{-15.35\%}$	$848^{+7.37\%}_{-13.70\%}$
	14	$90.10^{+7.34\%}_{-15.13\%}$	$1011^{+7.24\%}_{-13.39\%}$
$\sigma^{LO}(tHW)(fb)$ [48]	13	$15.77^{+15.91\%}_{-15.76\%}$	-
$\sigma^{NLO}DR1(tHW)(fb)$ [48]	13	$21.72^{+6.52\%}_{-5.24\%}$	≈ 150
$\sigma^{NLO}DR2(tHW)(fb)$ [48]	13	$16.28^{+7.34\%}_{-15.13\%}$	≈ 150

Table 2.11: Predicted enhancement of the tHq and tHW cross sections at LHC for $\kappa_V = 1$ and $\kappa_t = \pm 1$ at LO and NLO; the cross section enhancement of more than a factor of 10 is due to the flippling in the sign of the H-t coupling with respect to the SM one.

812 2.5 The CP-mixing in tH processes

813 In addition to the sensitivity to sign of the H-t coupling, tHq and tHW processes have
 814 been proposed as a tool to investigate the possibility of a H-t coupling that does not
 815 conserve CP [43, 48, 50]. Current experimental results are consistent with SM H-V
 816 and H-t couplings; however, negative H-t coupling is not excluded completely [52].

817

818 In this thesis, the sensitivity of th processes to CP-mixing is also studied in the
 819 effective field theory framework and based in references [43, 48]; a generic particle
 820 (X_0) of spin-0 and a general CP violating interaction with the top quark, can couple
 821 to scalar and pseudoscalar fermionic densities. The H-W interaction is assumed to
 822 be SM-like. The Lagrangian modeling the H-t interaction is given by

$$\mathcal{L}_0^t = -\bar{\psi}_t (c_\alpha \kappa_{Htt} g_{Htt} + i s_\alpha \kappa_{Att} g_{Att} \gamma_5) \psi_t X_0, \quad (2.58)$$

823 where α is the CP-mixing phase, $c_\alpha \equiv \cos \alpha$ and $s_\alpha \equiv \sin \alpha$, κ_{Htt} and κ_{Att} are real
 824 dimensionless rescaling parameters⁹, $g_{Htt} = g_{Att} = m_t/v = y_t/\sqrt{2}$ and $v \sim 246$ GeV is
 825 the Higgs vacuum expectation value. In this parametrization, it is easy to recover
 826 three special cases

- 827 • CP-even coupling $\rightarrow \alpha = 0^\circ$
- 828 • CP-odd coupling $\rightarrow \alpha = 90^\circ$
- 829 • SM coupling $\rightarrow \alpha = 0^\circ$ and $\kappa_{Htt} = 1$

830 The loop induced X_0 coupling to gluons can also be described in terms of the
 831 parametrization above, according to

$$\mathcal{L}_0^g = -\frac{1}{4} \left(c_\alpha \kappa_{Hgg} g_{Hgg} G_{\mu\nu}^a G^{a,\mu\nu} + s_\alpha \kappa_{Agg} g_{Agg} G_{\mu\nu}^a \tilde{G}^{a,\mu\nu} \right) X_0. \quad (2.59)$$

832 where $g_{Hgg} = -\alpha_s/3\pi v$ and $g_{Agg} = \alpha_s/2\pi v$. Under the assumption that the top quark
 833 dominates the gluon-fusion process at LHC energies, $\kappa_{Hgg} \rightarrow \kappa_{Htt}$ and $\kappa_{Agg} \rightarrow \kappa_{Att}$,
 834 so that the ratio between the gluon-gluon fusion cross section for X_0 and for the SM
 835 Higgs prediction can be written as

$$\frac{\sigma_{NLO}^{gg \rightarrow X_0}}{\sigma_{NLO,SM}^{gg \rightarrow H}} = c_\alpha^2 \kappa_{Htt}^2 + s_\alpha^2 \left(\kappa_{Att} \frac{g_{Agg}}{g_{Hgg}} \right)^2. \quad (2.60)$$

836 If the rescaling parameters are set to

$$\kappa_{Htt} = 1, \quad \kappa_{Att} = \left| \frac{g_{Hgg}}{g_{Agg}} \right| = \frac{2}{3}. \quad (2.61)$$

837 the gluon-fusion SM cross section is reproduced for every value of the CP-mixing
 838 angle α ; therefore, by imposing that condition to the Lagrangian density 2.58, the

⁹ analog to κ_t and κ_V

CP-mixing angle is not constrained by current data. Figure 2.16 shows the NLO cross sections for t-channel tX_0 (blue) and $t\bar{t}X_0$ (red) associated production processes as a function of the CP-mixing angle α . X_0 is a generic spin-0 particle with top quark CP-violating coupling. Rescaling factors κ_{Htt} and κ_{Att} have been set to reproduce the SM gluon-fusion cross sections.

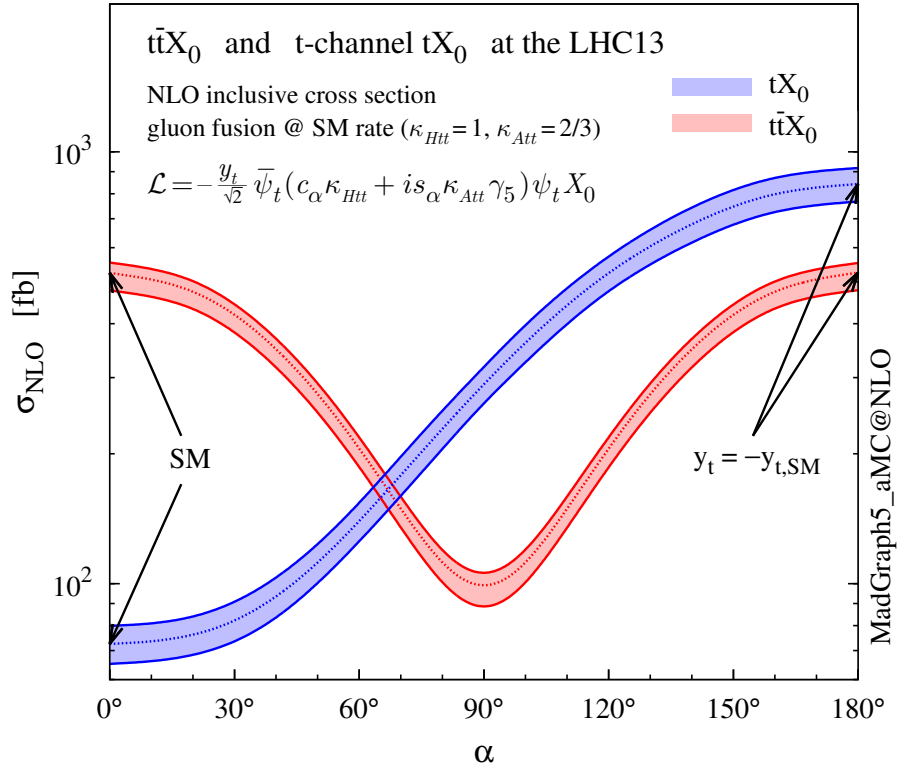


Figure 2.16: NLO cross sections for t-channel tX_0 (blue) and $t\bar{t}X_0$ (red) associated production processeses as a function of the CP-mixing angle α . X_0 is a generic spin-0 particle with top quark CP-violating coupling [43].

It is interesting to notice that the tX_0 croos section is enhanced, by a factor of about 10, when a continuous rotation in the scalar-pseudoscalar plane is applied; this enhancement is similar to the enhancement produced when the H-t coupling is flipped in sign with respect to the SM ($y_t = -y_{t,SM}$ in the plot), as showed in section 2.4. In contrast, the degeneracy in the $t\bar{t}X_0$ cross section is still present given that it depends

quadratically on the H-t coupling, but more interesting is to notice that $t\bar{t}X_0$ cross section is exceeded by tX_0 cross section after $\alpha \sim 60^\circ$.

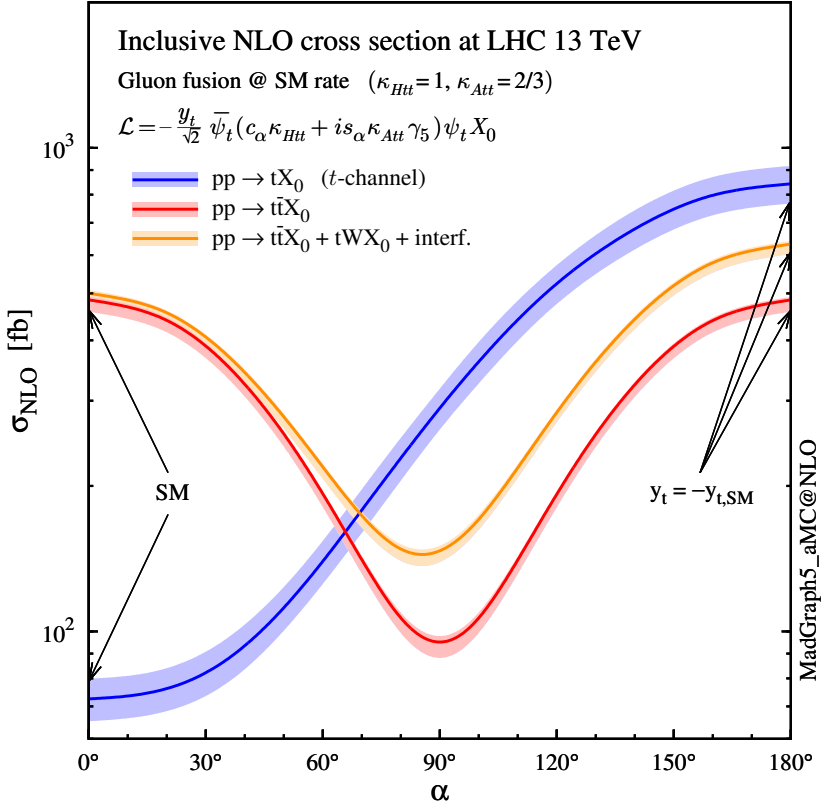


Figure 2.17: NLO cross sections for t-channel tX_0 (blue), $t\bar{t}X_0$ (red) associated production processes and combined $tWX_0 + t\bar{t}X_0$ (including interference) production as a function of the CP-mixing angle α [43].

850

851 A similar parametrization can be used to investigate the tHW process sensitivity to
 852 CP-violating H-t coupling. As said in 2.4, the interference in the W-associated chan-
 853 nel is more complicated because there are more than two contributions and also there
 854 is interference with the $t\bar{t}H$ production process.

855

856 Figure 2.17 shows the NLO cross sections for t-channel tX_0 (blue), $t\bar{t}X_0$ (red) asso-
 857 ciated production and for the combined $tWX_0 + t\bar{t}X_0 +$ interference (orange) as a
 858 function of the CP-mixing angle. It is clear that the effect of the interference in the

combined case is the lifting of the degeneracy present in the $t\bar{t}X_0$ production. The constructive interference enhances the cross section from about 500 fb at SM ($\alpha = 0$) to about 600 fb ($\alpha = 180^\circ \rightarrow y_t = -y_{t,SM}$).

An analysis combining tHq and tHW processes will be made in this thesis taking advantage of the sensitivity improvement.

2.6 Experimantal status of the anomalous Higg-fermion coupling.

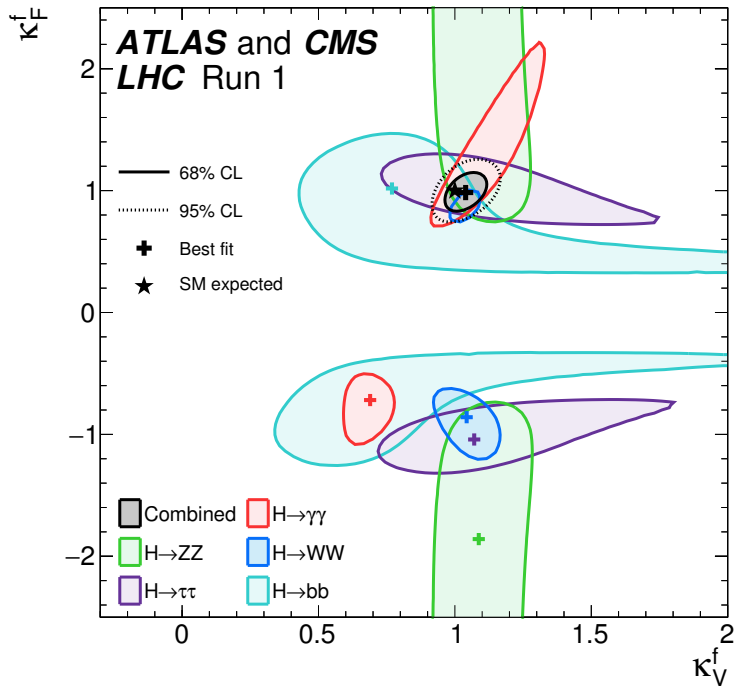


Figure 2.18: Combination of the ATLAS and CMS fits for coupling modifiers κ_t - κ_V ; also shown the individual decay channels combination and their global combination. No assumptions have been made on the sign of the coupling modifiers [52].

ATLAS and CMS have performed analysis of the anomalous H-f coupling by making likelihood scans for the two coupling modifiers, κ_t and κ_V , under the assumption that

868 $\kappa_Z = \kappa_W = \kappa_V$ and $\kappa_t = \kappa_\tau = \kappa_b = \kappa_f$. Figure 2.18 shows the result of the combination
869 of ATLAS and CMS fits; also the individual decay channels combination and the
870 global combination results are shown.

871 While all the channels are compatible for positive values of the modifiers, for negative
872 values of κ_t there is no compatibility. The best fit for individual channels is compatible
873 with negative values of κ_t except for the $H \rightarrow bb$ channel which is expected to be the
874 most sensitive channel; therefore, the best fit for the global fit yields $\kappa_t \geq 0$. Thus,
875 the anomalous H-t coupling cannot be excluded completely.

⁸⁷⁶ **Chapter 3**

⁸⁷⁷ **The CMS experiment at the LHC**

⁸⁷⁸ **3.1 Introduction**

⁸⁷⁹ Located on the Swiss-French border, the European Council for Nuclear Research
⁸⁸⁰ (CERN) the largest scientific organization leading the particle physics research.
⁸⁸¹ About 13000 people in a broad range of fields including users, students, scientists,
⁸⁸² engineers among others, contribute to the data taking and analysis, with the goal
⁸⁸³ of unveiling the secrets of nature and revealing the fundamental structure of the
⁸⁸⁴ universe. CERN is also the home of the Large Hadron Collider (LHC), the largest
⁸⁸⁵ circular particle accelerator around the world, where protons (or heavy ions) traveling
⁸⁸⁶ close to the speed of light, are made to collide. These collisions open a window
⁸⁸⁷ to investigate how particles (and their constituents if they are composite) interact
⁸⁸⁸ with each other, providing clues about the laws of nature. This chapter presents an
⁸⁸⁹ overview of the LHC structure and operation. A detailed description of the CMS
⁸⁹⁰ detector is offered, given that the data used in this thesis have been taken with this
⁸⁹¹ detector.

892 **3.2 The LHC**

893 With 27 km of circumference, the LHC is currently the largest and most powerful
 894 circular accelerator in the world. It is installed in the same tunnel where the Large
 895 Electron-Positron (LEP) collider was located, taking advantage of the existing infras-
 896 tructure. The LHC is also the larger accelerator in the CERN's accelerator complex
 897 and is assisted by several successive accelerating stages before the particles are in-
 898 jected into the LHC ring where they reach their maximum energy (see figure 3.1).

Figure 3.1: CERN accelerator complex. Blue arrows show the path followed by protons along the acceleration process [53].

899 LHC runs in three modes depending on the particles being accelerated

- 900 ● Proton-Proton collisions (pp) for multiple physics experiments.
- 901 ● Lead-Lead collisions ($Pb-Pb$) for heavy ion experiments.
- 902 ● Proton-Lead collisions ($p-Pb$) for quark-gluon plasma experiments.

903 In this thesis  collisions will be considered.

904

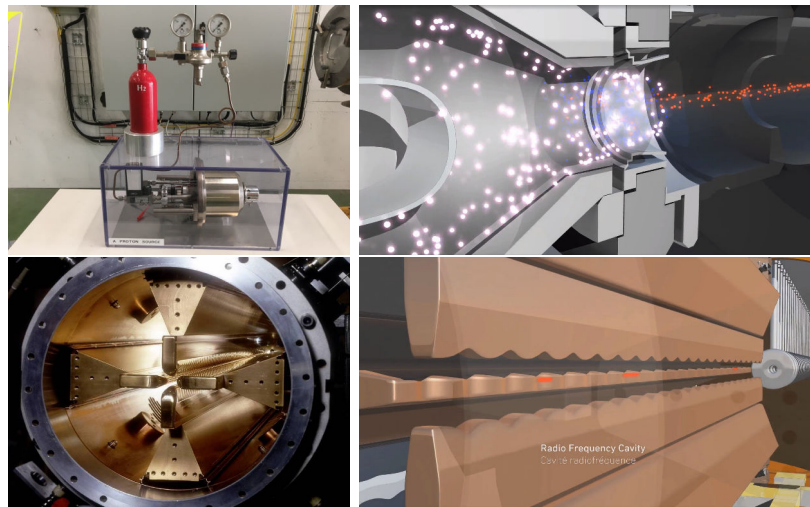


Figure 3.2: LHC protons source and the first acceleration stage. Top: the bottle contains hydrogen gas (white dots) which is injected into the metal cylinder to be broken down into electrons(blue dots) and protons(red dots); Bottom: the obtained protons are directed towards the radio frequency quadrupole which perform the first acceleration, focus the beam and create the bunches of protons. [57,58]

905 Collection of protons starts with hydrogen atoms taken from a bottle, containing hy-
 906 drogen gas, and injecting them in a metal cylinder; hydrogen atoms are broken down
 907 into electrons and protons by an intense electric field (see figure3.2 top). The result-
 908 ing protons leave the metal cylinder towards a radio frequency quadrupole (RFQ)
 909 that focus the beam, accelerates the protons and creates the packets of protons called
 910 bunches. In the RFQ, an electric field is generated by a RF wave at a frequency that
 911 matches the resonance frequency of the cavity where the electrodes are contained.
 912 The beam of protons traveling on the RFQ axis experiences an alternating electric
 913 field gradient that generates the focusing forces.

914

915 In order to accelerate the protons, a longitudinal time-varying electric field component
 916 is added to the system; it is done by giving the electrodes a sinus-like profile as shown
 917 in figure 3.2 bottom. By matching the speed and phase of the protons with the
 918 longitudinal electric field the bunching is performed; protons synchronized with the

919 RFQ (synchronous proton) do not feel an accelerating force, but those protons in the
 920 beam that have more (or less) energy than the synchronous proton (asynchronous
 921 protons) will feel a decelerating (accelerating) force; therefore, asynchronous protons
 922 will oscillate around the synchronous ones forming bunches of protons [55]. From the
 923 RFQ protons emerge with energy 750 keV in bunches of about 1.15×10^{11} protons [56].

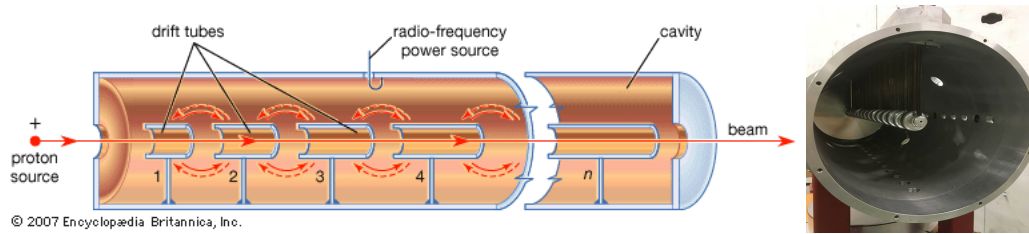


Figure 3.3: The LINAC2 accelerating system at CERN. Electric fields generated by radio frequency (RF) create acceleration and deceleration zones inside the cavity; deceleration zones are blocked by drift tubes where quadrupole magnets focus the proton beam. [59]

924 Proton bunches coming from the RFQ go to the linear accelerator 2 (LINAC2) where
 925 they are accelerated to reach 50 MeV energy. In the LINAC2 stage, acceleration
 926 is performed using electric fields generated by radio frequency which create zones
 927 of acceleration and deceleration as shown in figure 3.3. In the decelerations zones,
 928 the electric field is blocked using drift tubes where protons are free to drift while
 929 quadrupole magnets focus the beam.

930

931 The beam coming from LINAC2 is injected into the proton synchrotron booster
 932 (PSB) to reach 1.4 GeV in energy. The next acceleration is provided at the pro-
 933 ton synchrotron (PS) up to 26 GeV, followed by the injection into the super proton
 934 synchrotron (SPS) where protons are accelerated to 450 GeV. Finally, protons are
 935 injected into the LHC where they are accelerated to the target energy of 6.5 TeV.
 936 PSB, PS, SPS and LHC accelerate protons using the same RF acceleration technic
 937 described before.

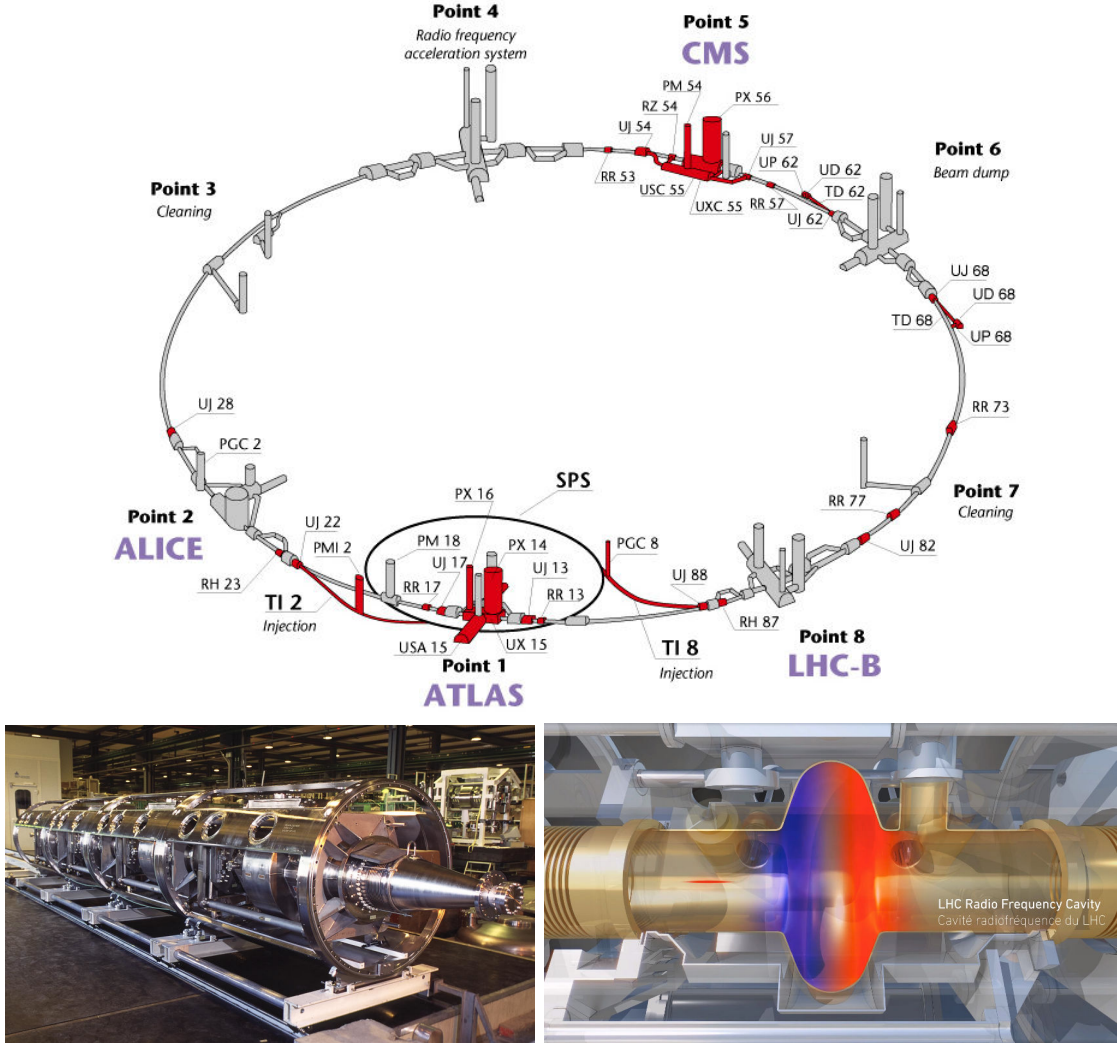


Figure 3.4: Top: LHC layout. The red zones indicate the infrastructure additions to the LEP installations, built to accommodate the ATLAS and CMS experiments which exceed the size of the former experiments located there [54]. Bottom: LHC RF cavities. A module accommodates 4 cavities that accelerate protons and preserve the bunch structure of the beam. [58, 60]

938 LHC has a system of 16 RF cavities located in the so-called point 4, as shown in
 939 figure 3.4 top, tuned at a frequency of 400 MHz and the protons are carefully timed 
 940 so in addition to the acceleration effect the bunch structure of the beam is preserved.
 941 Bottom side of figure 3.4 shows a picture of a RF module composed of 4 RF cavities
 942 working in a superconducting state at 4.5 K; also is showed a representation of the

943 accelerating electric field that accelerates the protons in the bunch.

944

945 While protons are accelerated in one section of the LHC ring, where the RF cavities
 946 are located, in the rest of their path they have to be kept in the curved trajectory
 947 defined by the LHC ring. Technically, LHC is not a perfect circle; RF, injection, beam
 948 dumping, beam cleaning and sections before and after the experimental points where
 949 protons collide are all straight sections. In total, there are 8 arcs 2.45 Km long each
 950 and 8 straight sections 545 m long each. In order to curve the proton's trajectory in
 951 the arc sections, superconducting dipole magnets are used.

952

953 Inside the LHC ring, there are two proton beams traveling in opposite directions in
 954 two separated beam pipes; the beam pipes are kept at ultra-high vacuum ($\sim 10^{-9}$
 955 Pa) to ensure that there are no particles that interact with the proton beams. The
 956 superconducting dipole magnets used in LHC are made of a NbTi alloy, capable of
 957 transporting currents of about 12000 A when cooled at a temperature below 2K using
 958 liquid helium (see figure 3.5).

959

960 Protons in the arc sections of LHC feel a centripetal force exerted by the dipole
 961 magnets which is perpendicular to the beam trajectory; The magnitude of magnetic
 962 field needed can be found assuming that protons travel at $v \approx c$, using the standard
 963 values for proton mass and charge and the LHC radius, as

$$F_m = \frac{mv^2}{r} = qBv \quad \rightarrow B = 8.33T \quad (3.1)$$

964 which is about 100000 times the Earth's magnetic field. A representation of the mag-
 965 netic field generated by the dipole magnets is shown on the bottom left side of figure

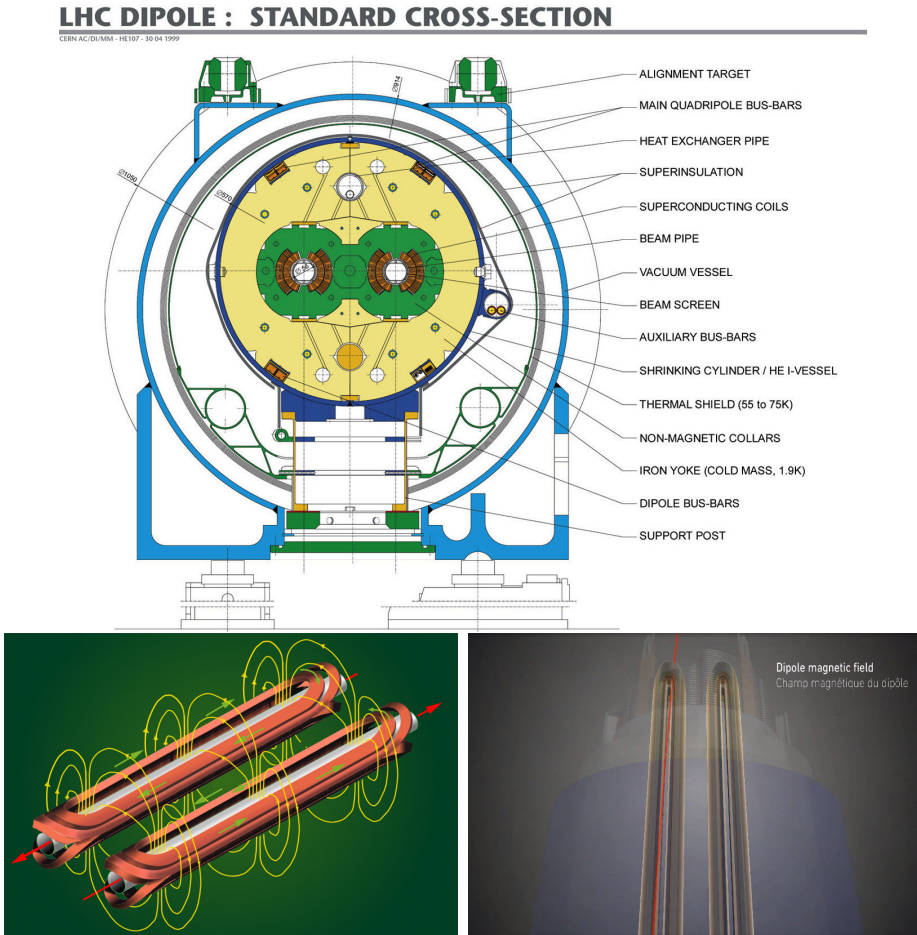


Figure 3.5: Top: LHC dipole magnet transversal view; cooling, shielding and mechanical support are indicated. Bottom left: Magnetic field generated by the dipole magnets; note that the direction of the field inside one beam pipe is opposite with respect to the other beam pipe which guarantee that both proton beams are curved in the same direction towards the center of the ring. The effect of the dipole magnetic field on the proton beam is represented on the bottom right side [58, 61, 62].

966 3.5. The bending effect of the magnetic field on the proton beam is shown on the
 967 bottom right side of figure 3.5. Note that the dipole magnets are not curved; the arc
 968 section of the LHC ring is composed of straight dipole magnets of about 15 m. In
 969 total there are 1232 dipole magnets along the LHC ring.

970

971 In addition to bending the beam trajectory, the beam has to be focused so it stays

972 inside the beam pipe. The focusing is performed by quadrupole magnets installed in
 973 a different straight section; in total 858 quadrupole magnets are installed along the
 974 LHC ring. Other effects like electromagnetic interaction among bunches, interaction
 975 with electron clouds from the beam pipe, the gravitational force on the protons, dif-
 976 ferences in energy among protons in the same bunch, among others, are corrected
 977 using sextupole and other magnetic multipoles.

978

979 The two proton beams inside the LHC ring are made of bunches with a cylindrical
 980 shape of about 7.5 cm long and about 1 mm in diameter; when bunches are close
 981 to the collision point (CP), the beam is focused up to a diameter of about 16 μm in
 982 order to maximize the number of collisions per unit area and per second, known as
 983 luminosity (L). Luminosity can be calculated using

$$L = fn \frac{N_1 N_2}{4\pi\sigma_x\sigma_y} \quad (3.2)$$

984 where f is the revolution frequency, n is the number of bunches per beam, N_1 and
 985 N_2 are the numbers of protons per bunch (1.5×10^{11}), σ_x and σ_y are the gaussian
 986 transverse sizes of the bunches. The expected luminosity  put

$$f = \frac{v}{2\pi r_{LHC}} \approx \frac{3 \times 10^8 \text{ m/s}}{27 \text{ km}} \approx 11.1 \text{ kHz},$$

$$n = 2808$$

$$N_1 = N_2 = 1.5 \times 10^{11}$$

$$\sigma_x = \sigma_y = 16 \mu\text{m}$$

987

$$L = 1.28 \times 10^{34} \text{ cm}^{-2} \text{ s}^{-1} = 1.28 \times 10^{-5} \text{ fb}^{-1} \text{ s}^{-1} \quad (3.3)$$

988 Luminosity is a fundamental aspect of LHC given that the bigger luminosity the bigger
 989 number of collisions, which means that for processes with a very small cross section
 990 the number of expected occurrences is increased and so the chances of being detected.
 991 The integrated luminosity, i.e. the total luminosity, collected by the CMS experiment
 992 during 2016 is shown in figure 3.6; the data analyzed in this thesis corresponds to an
 993 integrated luminosity of 35.9 fb^{-1} at a center of mass-energy $\sqrt{s} = 13 \text{ TeV}$.
 994 A way to increase L is increasing the number of bunches in the beam. Currently, the
 995 separation between two consecutive bunches in the beam is 7.5 m which corresponds
 996 to a time separation of 25 ns. In the full LHC ring the allowed number of bunches is
 997 $n = 27\text{km}/7.5\text{m} = 3600$; however, there are some gaps in the bunch pattern intended
 998 for preparing the dumping and injection of the beam, thus, the proton beams are
 999 composed of 2808 bunches.

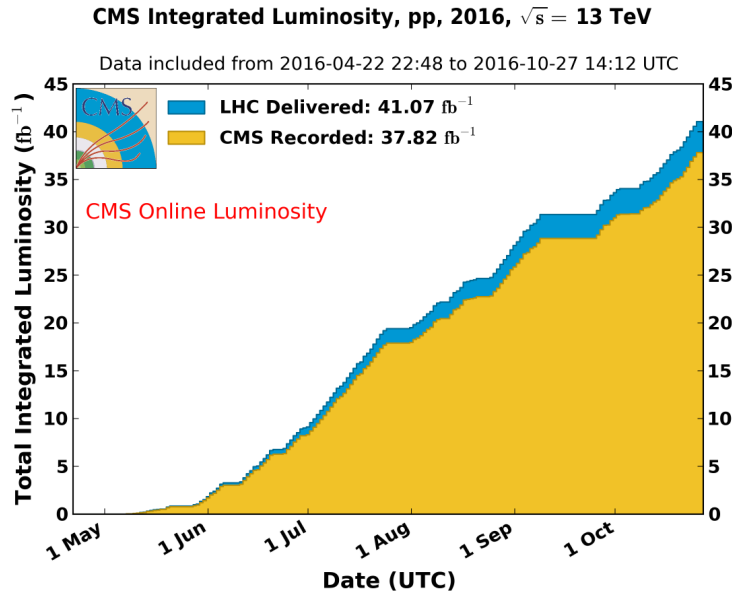


Figure 3.6: Integrated luminosity delivered by LHC and recorded by CMS during 2016. The difference between the delivered and the recorded luminosities is due to fails and issues occurred during the data taking in the CMS experiment [63].

1000 Once the proton beams reach the desired energy, they are brought to cross each other

1001 producing proton-proton collisions. The bunch crossing happens in precise places
 1002 where the four LHC experiments are located, as seen in figure 3.7 left. In 2008, the
 1003 first set of collisions involved protons with $\sqrt{s} = 7$ TeV; the energy was increased to
 1004 8 TeV in 2012 and to 13 TeV in 2015.

1005 CMS and ATLAS experiments, which are multi-purpose experiments, are enabled
 1006 to explore physics in any of the collision modes. LHCb experiment is optimized
 1007 to explore bottom quark physics, while ALICE is optimized for heavy ion collisions
 1008 searches; TOTEM and LHCf are dedicated to forward physics studies; MoEDAL (not
 1009 indicated in the figure) is intended for monopoles or massive pseudo stable particles
 1010 searches.

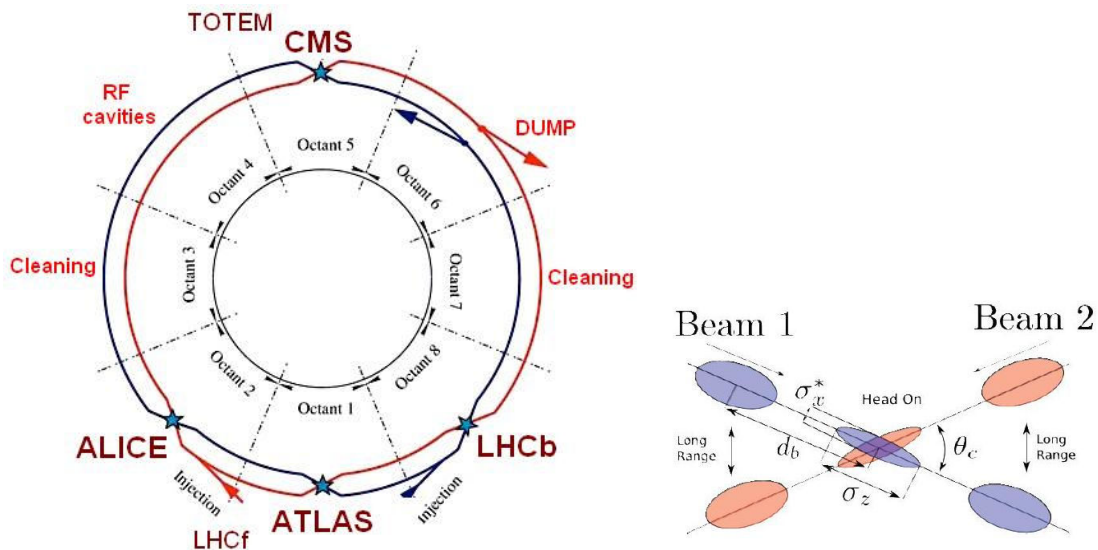


Figure 3.7: Left: LHC interaction points. Bunch crossing occurs where the LHC experiments are located [64]. Sections indicated as cleaning are dedicated to collimate the beam in order to protect the LHC ring from collisions with protons in very spreaded bunches. Right: bunch crossing scheme. Since the bunch crossing is not perfectly head-on, the luminosity is reduced in a factor of 17%.

1011 At the CP there are two interesting details that need to be addressed. The first
 1012 one is that the bunch crossing does not occur head-on but at a small crossing angle
 1013 ($280 \mu\text{rad}$ in CMS and ATLAS) as shown in the right side of figure 3.7, affecting the

1014 overlapping between bunches; the consequence is a reduction of about 17% in the
 1015 luminosity. The second one is the occurrence of multiple pp collisions in the same
 1016 bunch crossing; this effect is called pile-up (PU). A fairly simple estimation of the
 1017 PU follows from estimating the probability of collision between two protons, one from
 1018 each of the bunches in course of collision; it depends roughly on the ratio of proton
 1019 size and the cross section of the bunch in the interaction point, i.e.,

$$P(pp\text{-}collision) \sim \frac{d_{proton}^2}{\sigma_x \sigma_y} = \frac{(1\text{fm})^2}{(16\mu\text{m})^2} \sim 4 \times 10^{-21} \quad (3.4)$$

1020 however, there are $N = 1.15 \times 10^{11}$ protons in a bunch, thus the estimated number of
 1021 collisions in a bunch crossing is

$$PU = N^2 * P(pp\text{-}collision) \sim 50 \text{ pp-collision per bunch crossing}, \quad (3.5)$$

1022 about 20 of those pp collisions are inelastic. Each collision generates a vertex, but
 1023 only the most energetic is considered as a primary vertex; the rest are considered as
 1024 PU vertices. A multiple pp collision event in a bunch crossing at CMS is showed in
 1025 figure3.8. Unstable particles outgoing from the primary vertex will eventually decay;
 1026 this decay vertex is known as a secondary vertex.
 1027 Next section presents a description of the CMS detector which it is the detector used
 1028 to collect the data used in this thesis.

1029 3.3 The CMS experiment

1030 CMS is a general-purpose detector designed to conduct research in a wide range
 1031 of physics from the standard model to new physics like extra dimensions and dark

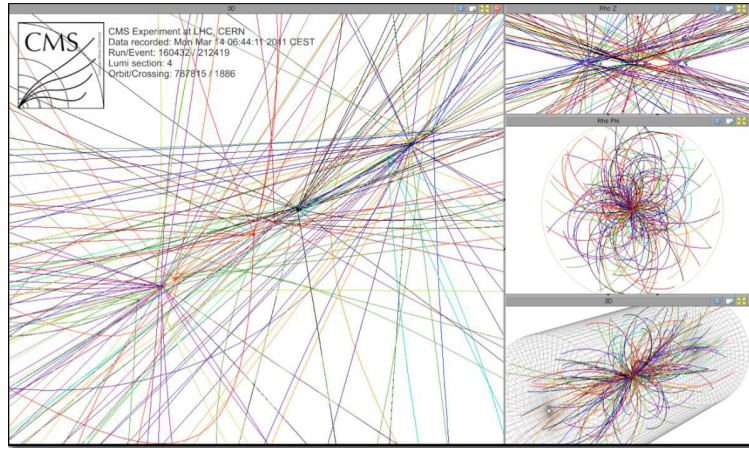


Figure 3.8: Multiple pp collision bunch crossing at CMS. Only the most energetic vertex is considered and the rets are cataloged as PU vertices [65].

matter. Located at the point 5 in the LHC layout as shown in figure 3.4, CMS is composed of several detection systems distributed in a cylindrical structure; in total, CMS weights about 12500 tons in a very compact 21.6 m long and 14.6 m diameter cylinder. It was built in 15 separate sections at the ground level and lowered to the cavern individually to be assembled. A complete and detailed description of the CMS detector and its components is given in reference [66] on which this section is based on.

1038

1039 Figure 3.9 shows the layout of the CMS detector. The design is driven by the requirements on the identification, momentum resolution and unambiguous charge determination of the muons; therefore, a large bending power is provided by the solenoid magnet made of superconducting cable capable to generate a 3.8 T magnetic field.

1040 1041 1042 1043

The detection system is composed of (from the innermost to the outermost)

1044 • Pixel detector.

1045 • Silicon strip tracker.

1046 • Preshower detector.

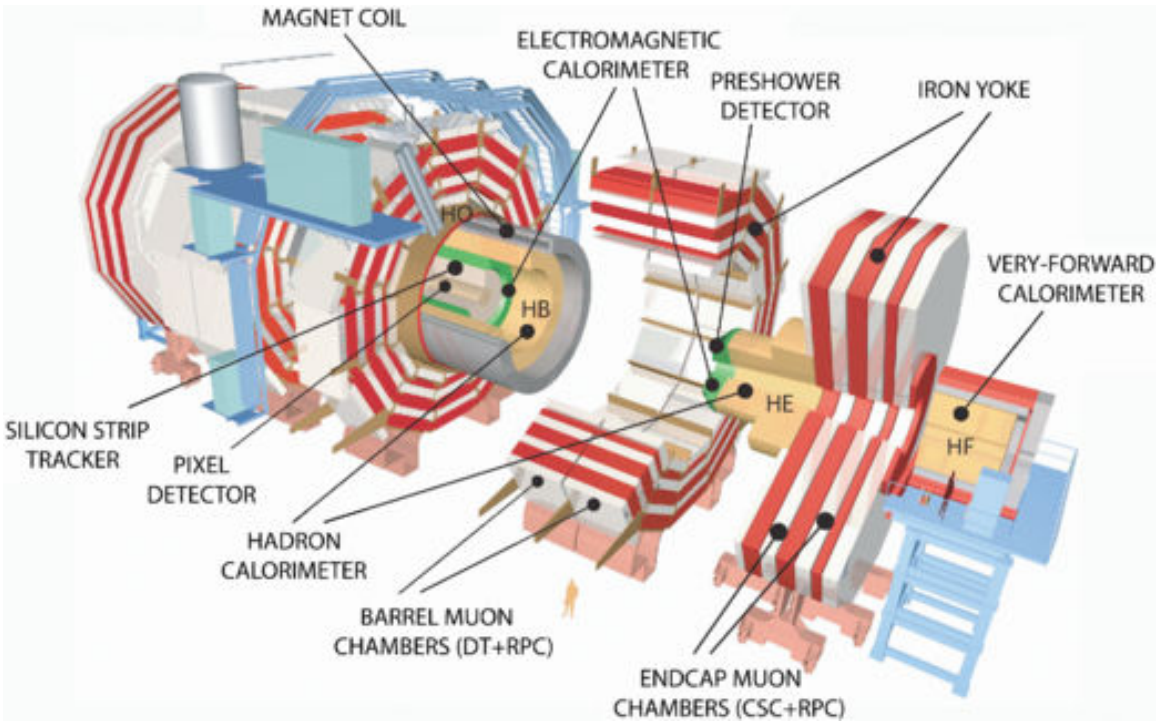


Figure 3.9: Layout of the CMS detector. The several subdetectors are indicated. The central region of the detector is referred as the Barrel section while the endcaps are referred as the forward sections. [67].

1047 • Electromagnetic calorimeter.

1048 • Hadronic calorimeter.

1049 • Muon chambers (Barrel and endcap)

1050 The central region of the detector is commonly referred as the barrel section while the
 1051 endcaps are referred as the forward sections of the detector; thus, each subdetector
 1052 is composed of a barrel section and a forward section.

1053 3.3.1 Coordinate system

1054 The coordinate system used by CMS is centered in the geometrical center of the
 1055 detector which is the same as the CP as shown in figure 3.10. The z -axis is parallel

1056 to the beam direction, while the Y -axis pointing vertically upward, and the X -axis
 1057 pointing radially inward toward the center of the LHC.

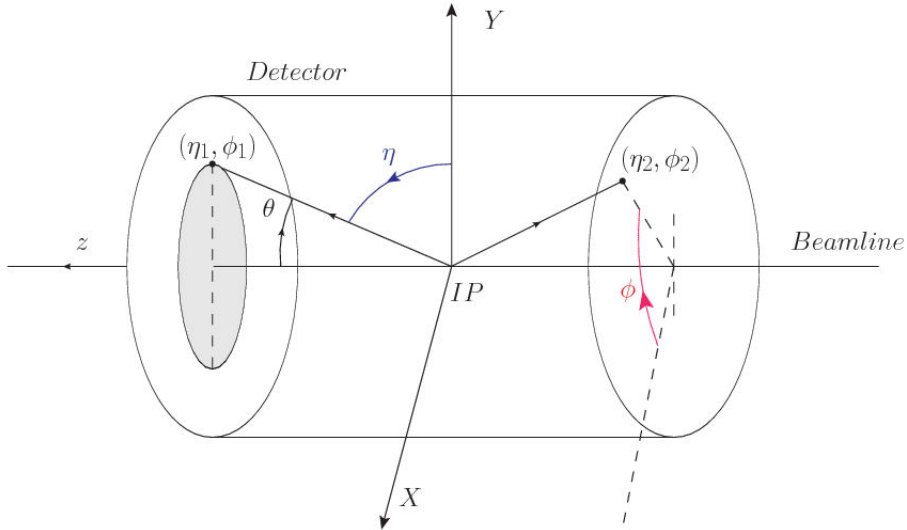


Figure 3.10: CMS detector coordinate system.

1058 In addition to the common cartesian and cylindrical coordinate systems, two coordi-
 1059 nates are of particular utility in particle physics: rapidity(y) and pseudorapidity(η),
 1060 defined in connection to the polar angle θ , energy and longitudinal momentum com-
 1061 ponent (momentum along the z -axis) according to

$$y = \frac{1}{2} \ln \frac{E + p_z}{E - p_z} \quad \eta = -\ln \left(\tan \frac{\theta}{2} \right) \quad (3.6)$$

1062 Rapidity is related to the angle between the XY -plane and the direction in which the
 1063 products of a collision are emitted; it has the nice property that the difference between
 1064 the rapidities of two particles is invariant with respect to Lorentz boosts along the z -
 1065 axis. Thus, data analysis becomes more simple when based on rapidity; however, it is
 1066 not simple to measure the rapidity of highly relativistic particles, as those produced
 1067 after pp collisions. Under the highly relativistic motion approximation, y can be
 1068 rewritten in terms of the polar angle, concluding that rapidity is approximately equal

1069 to the pseudorapidity defined above, i.e. $y \approx \eta$. Note that η is easier to measure than y
 1070 given the direct relationship between the former and the polar angle. Angular distance
 1071 between two objects in the detector (ΔR) is defined in terms of their coordinates
 1072 $(\eta_1, \phi_1), (\eta_2, \phi_2)$ as

$$\Delta R = \sqrt{(\Delta\eta)^2 - (\Delta\phi)^2} \quad (3.7)$$

1073 **3.3.2 Pixels detector**

1074 The CMS tracking system is designed to provide a precise measurement of the trajectory
 1075 followed by the charged particles created after the pp collisions; also, the precise
 1076 reconstruction of the primary and secondary vertices is expected in an environment
 1077 where, each 25 ns, the bunch crossing produce about 20 inelastic collisions and about
 1078 1000 particles. An increment in the luminosity is ongoing which implies that the PU
 1079 will increase accordingly.

1080

1081 The pixel detector was replaced during the 2016-2017 extended year-end technical
 1082 stop, due to the increasingly challenging operating conditions like the higher particle
 1083 flow and more radiation harsh environment, among others. The new one is responding
 1084 as expected, reinforcing its crucial role in the successful way to fulfill the new
 1085 LHC physics objectives after the discovery of the Higgs boson. The last chapter of
 1086 this thesis is dedicated to describe my contribution to the “Forward Pixel Phase 1
 1087 upgrade”.

1088

1089 The current pixel detector is composed of 1856 silicon pixel detector modules organized
 1090 in four-barrel layers in the central region and three disks in the forward region;
 1091 it is designed to record efficiently and with high precision, up to $10\mu\text{m}$ in the XY -

1092 plane and $20\mu\text{m}$ in the z -direction, the first four space-points near to the CP region
 1093 (see figure 3.11 left side) in the range $|\eta| \leq 2.5$. The first barrel layer is located at a
 1094 radius of 30 mm from the beamline, while the fourth layer is located at a radius of
 1095 160 mm closer to the strip tracker inner barrel layer (see section 3.3.3) in order to
 1096 reduce the rate of fake tracks. The high granularity of the detector is represented in
 1097 its about 123 Mpixels, each of size $100 \times 150\mu\text{m}^2$, which is almost twice the channels
 1098 of the old detector. The transverse momentum resolution of tracks can be measured
 1099 with a resolution of 1-2% for muons of $p_T = 100$ GeV.

1100

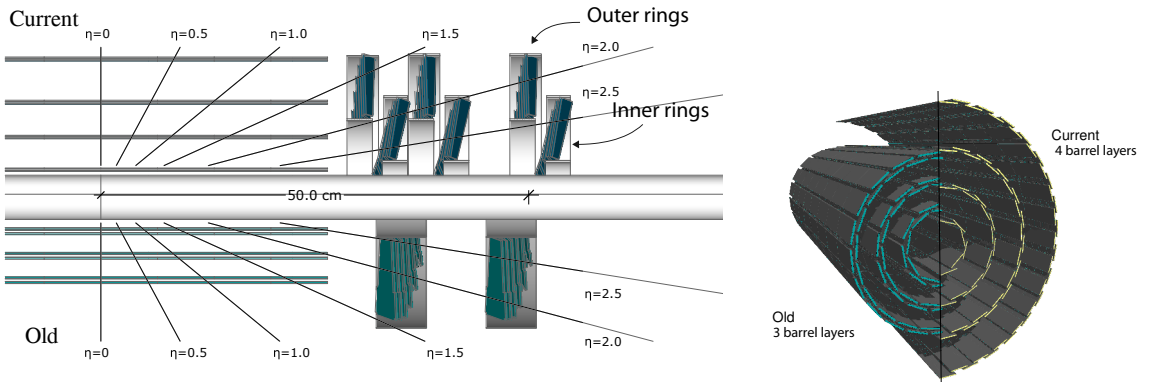


Figure 3.11: CMS pixel detector schematic view. Left: layout comparing the layers and disks in the old and current pixel detectors. Right: Transverse-oblique view comparing the pixel barrel layers in the two [69].

1101 Some of the improvements with respect to the previous pixel detector include a higher
 1102 average tracking efficiency and lower average fake rate as well as higher track impact
 1103 parameter resolution which is fundamental in order to increase the efficiency in the
 1104 identification of jets originating from b quarks (b-tagging). A significant source of
 1105 improvement comes from the overall reduction in the material budget of the detector
 1106 which results in fewer photon conversions and less multiple scattering from charged
 1107 particles.

1108 **3.3.3 Silicon strip tracker**

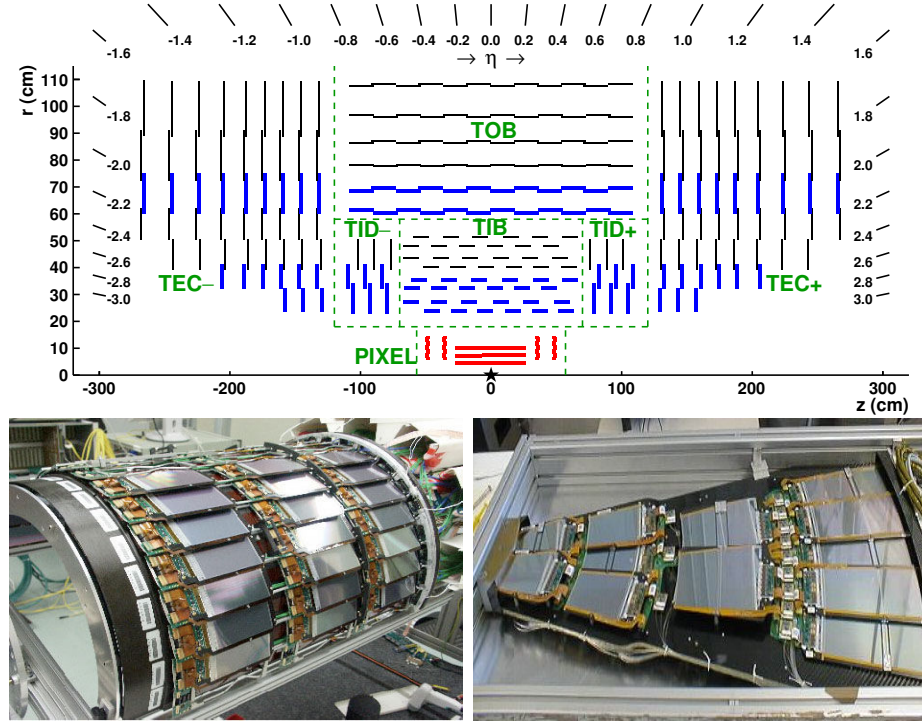


Figure 3.12: Top: CMS Silicon Strip Tracker (SST) schematic view. The SST is composed of the tracker inner barrel (TIB), the tracker inner disks (TID), the tracker outer barrel (TOB) and the tracker endcaps (TEC). Each part is made of silicon strip modules; the modules in blue represent two modules mounted back-to-back and rotated in the plane of the module by a stereo angle of 120 mrad in order to provide a 3-D reconstruction of the hit positions. Bottom: pictures of the TIB (left) and TEC (right) modules [70–72].

1109 The silicon strip tracker (SST) is the second stage in the CMS tracking system. The
 1110 top side of figure 3.12 shows a schematic of the SST. The inner tracker region is com-
 1111 posed of the tracker inner barrel (TIB) and the tracker inner disks (TID) covering the
 1112 region $r < 55$ cm and $|z| < 118$ cm. The TIB is composed of 4 layers while the TID
 1113 is composed of 3 disks at each end. The silicon sensors in the inner tracker are 320
 1114 μm thick, providing a resolution of about 13–38 μm in the $r\phi$ position measurement.
 1115
 1116 The modules indicated in blue in the schematic view of figure 3.12 are two modules

1117 mounted back-to-back and rotated in the plane of the module by a “stereo” angle of
 1118 100 mrad; the hits from these two modules, known as “stereo hits”, are combined to
 1119 provide a measurement of the second coordinate (z in the barrel and r on the disks)
 1120 allowing the reconstruction of hit positions in 3-D.

1121

1122 The outer tracker region is composed of the tracker outer barrel (TOB) and the
 1123 tracker endcaps (TEC). The six layers of the TOB offer coverage in the region $r > 55$
 1124 cm and $|z| < 118$ cm, while the 9 disks of the TEC cover the region $124 < |z| < 282$
 1125 cm. The resolution offered by the outer tracker is about $13\text{--}38 \mu\text{m}$ in the $r\phi$ position
 1126 measurement. The inner four TEC disks use silicon sensors $320 \mu\text{m}$ thick; those in
 1127 the TOB and the outer three TEC disks use silicon sensors of $500 \mu\text{m}$ thickness. The
 1128 silicon strips run parallel to the z -axis and the distance between strips varies from 80
 1129 μm in the inner TIB layers to $183 \mu\text{m}$ in the inner TOB layers; in the endcaps the
 1130 wedge-shaped sensors with radial strips, whose pitch range between $81 \mu\text{m}$ at small
 1131 radii and $205 \mu\text{m}$ at large radii.

1132

1133 The whole SST has 15148 silicon modules, 9.3 million silicon strips and cover a total
 1134 active area of about 198 m^2 .

1135 3.3.4 Electromagnetic calorimeter

1136 The CMS electromagnetic calorimeter (ECAL) is designed to measure the energy of
 1137 electrons and photons. It is composed of 75848 lead tungstate crystals which have a
 1138 short radiation length (0.89 cm) and fast response, since 80% of the light is emitted
 1139 within 25 ns; however, they are combined with Avalanche photodiodes (APDs) as
 1140 photodetectors given that crystals themselves have a low light yield ($30\gamma/\text{MeV}$). A

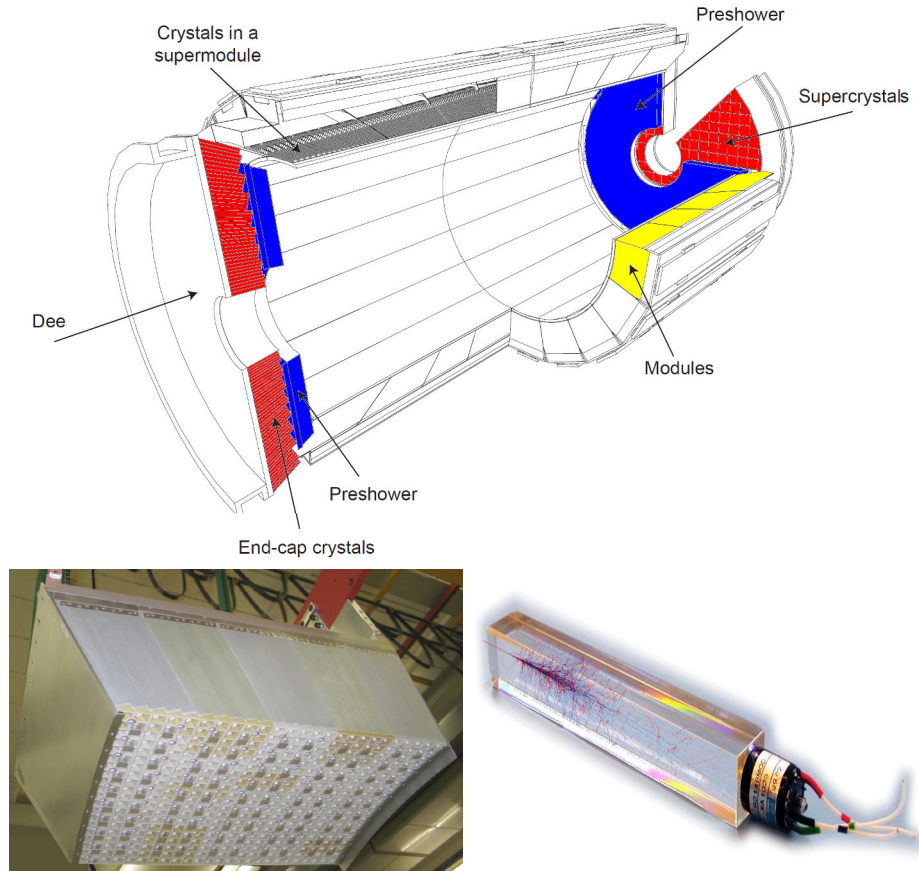


Figure 3.13: Top: CMS ECAL schematic view. Bottom: Module equipped with the crystals (left); ECAL crystal(right).

1141 schematic view of the ECAL is shown in figure 3.13.

1142

1143 Energy is measured by absorbing electrons and photons which generates an electro-
 1144 magnetic “shower”, as seen in bottom right picture of the figure3.13. The ECAL barrel
 1145 (EB) covers the region $|\eta| < 1.479$, using crystals of depth of 23 cm and $2.2 \times 2.2 \text{ cm}^2$
 1146 transverse section; the ECAL endcap (EE) covers the region $1.479 < |\eta| < 3.0$ using
 1147 crystals of depth 22 cm and transverse section of $2.86 \times 2.86 \text{ cm}^2$; the photodetectors
 1148 used are vacuum phototriodes (VPTs). Each EE is divided in two structures called
 1149 “Dees”.

1150

1151 In front of the EE, it is installed the preshower detector (ES) which covers the region
 1152 $1.65 < |\eta| < 2.6$. The ES provides a precise measurement of the position of electro-
 1153 magnetic showers, which allows to distinguish electrons and photons signals from π^0
 1154 decay signals. The ES is composed of a layer of lead absorber followed by a layer of
 1155 plastic scintillators

1156 **3.3.5 Hadronic calorimeter**

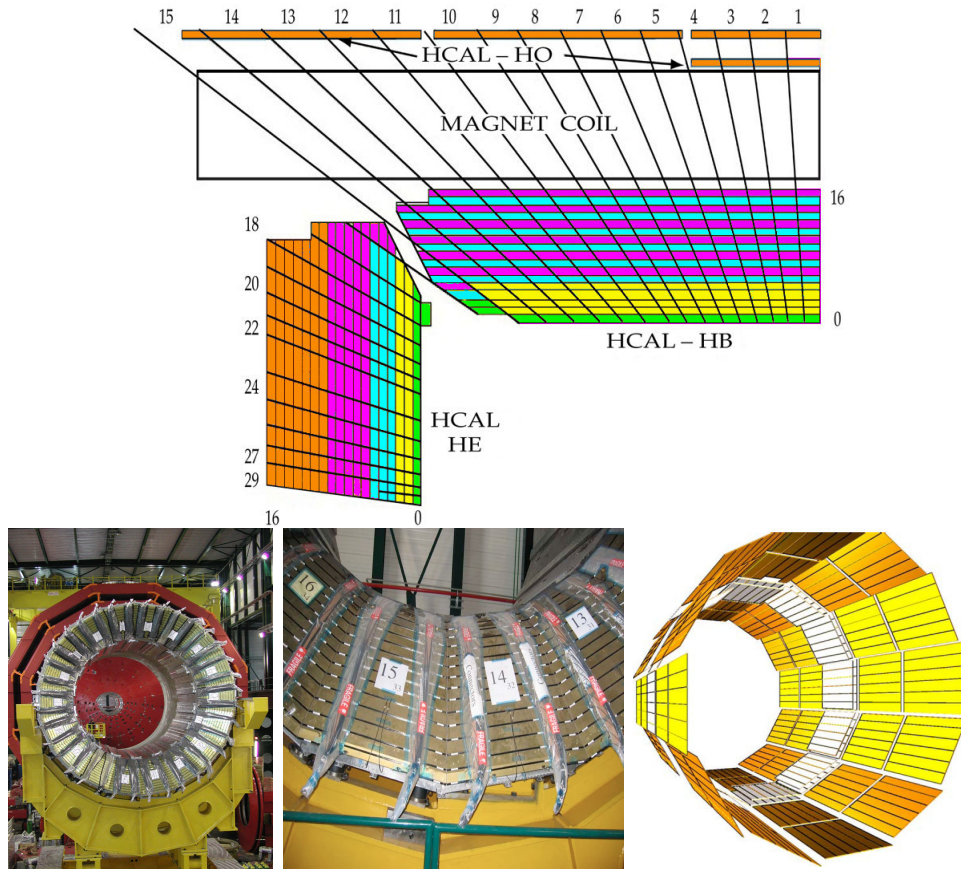


Figure 3.14: Top: CMS HCAL schematic view, the colors indicate the layers that are grouped into the same readout channels. Bottom: picture of a section of the HB; the absorber material is the golden region and scintillators are placed in between the absorber material (left and center). Schematic view of the HO (right). [73, 74]

1157 Hadrons are not absorbed by the ECAL but by the hadron calorimeter (HCAL),
 1158 which is made of a combination of alternating brass absorber layers and silicon photo-
 1159 multiplier(SiPM) layers; therefore, particles passing through the scintillator material
 1160 produce showers, as in the ECAL, as a result of the inelastic scattering of the hadrons
 1161 with the detector material. Since the particles are not absorbed in the scintillator,
 1162 their energy is sampled; therefore the total energy is not measured but estimated,
 1163 which reduce the resolution of the detector. Brass was chosen as the absorber mate-
 1164 rial due to its short interaction length ($\lambda_I = 16.42\text{cm}$) and its non-magnetivity. Figure
 1165 3.14 shows a schematic view of the CMS HCAL.

1166

1167 The HCAL is divided into four sections; the Hadron Barrel (HB), the Hadron Outer
 1168 (HO), the Hadron Endcap (HE) and the Hadron Forward (HF) sections. The HB
 1169 covers the region $0 < |\eta| < 1.4$, while the HE covers the region $1.3 < |\eta| < 3.0$. The HF,
 1170 made of quartz fiber scintillator and steel as absorption material, covers the forward
 1171 region $3.0 < |\eta| < 5.2$. Both the HB and HF are located inside the solenoid. The HO
 1172 is placed outside the magnet as an additional layer of scintillators with the purpose
 1173 of measure the energy tails of particles passing through the HB and the magnet (see
 1174 figure 3.14 top and bottom right). The upgrades made to the HCAL during the
 1175 technical stop 2016-2017 consisted in the replacement of the photo transducer, in
 1176 order to improve the efficiency.

1177 **3.3.6 Superconducting solenoid magnet**

1178 The superconducting magnet installed in the CMS detector is designed to provide
 1179 an intense and highly uniform magnetic field in the central part of the detector. In
 1180 fact, the tracking system takes advantage of the bending power of the magnetic field

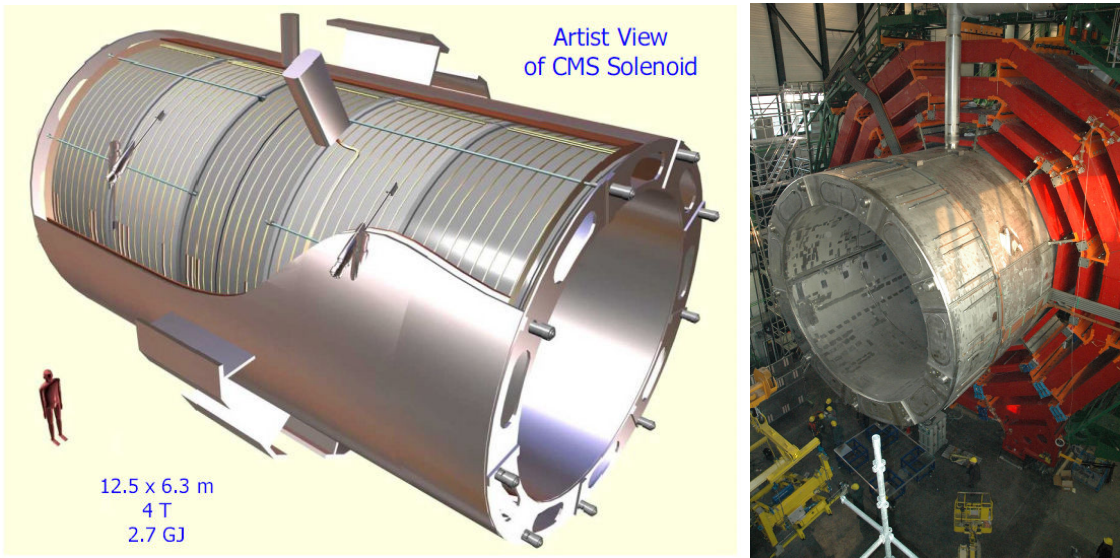


Figure 3.15: Artistic representation of the CMS solenoid magnet(left). The magnet is supported on an iron yoke (right) which also serves as the house of the muon detector and as mechanical support for the whole CMS detector [68].

1181 to measure with precision the momentum of the particles that traverse it; the unam-
 1182 biguous determination of the sign for high momentum muons was a driven principle
 1183 during the design of the magnet. The magnet has a diameter of 6.3 m, a length of 12.5
 1184 m and a cold mass of 220 t; the generated magnetic field reaches a strength of 3.8T.
 1185 Since it is made of Ni-Tb superconducting cable it has to operate at a temperature
 1186 of 4.7 K by using a helium cryogenic system; the current circulating in the cables
 1187 reaches 18800 A under normal running conditions. The left side of figure 3.15 shows
 1188 an artistic view of the CMS magnet, while the right side shows a transverse view of
 1189 the cold mass where the winding structure is visible.

1190
 1191 The yoke (see figure 3.15), composed of 5 barrel wheels and 6 endcap disks made
 1192 of iron, serves not only as the media for magnetic flux return but also provides the
 1193 house for the muon detector system and structural stability to the full detector.

1194 **3.3.7 Muon system**

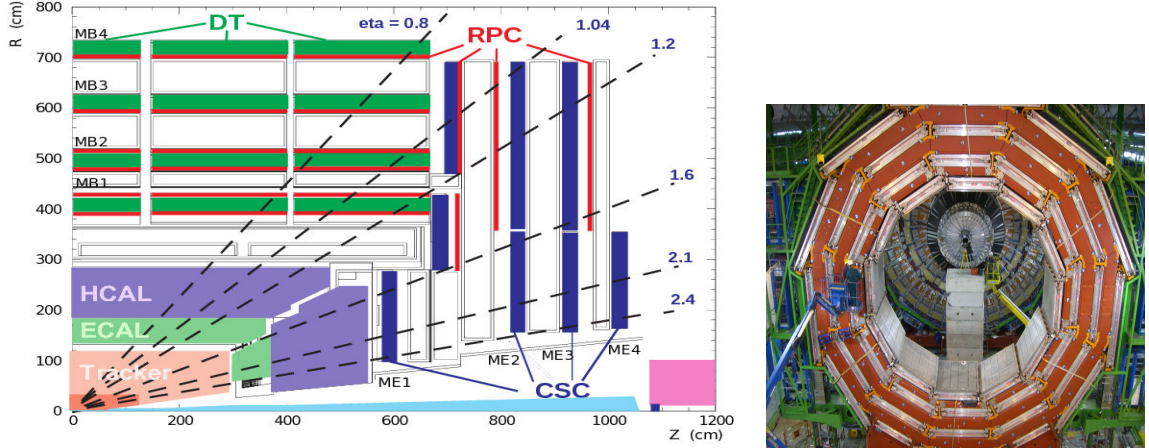


Figure 3.16: Left: CMS muon system schematic view; Right: one of the yoke rings with the muon DTs and RPCs installed; in the back it is possible to see the muon endcap [75].

1195 Muons are the only charged particles able to pass through all the CMS detector due
 1196 to their low ionization energy loss; thus, muons can be separated easily from the
 1197 high amount of particles produced in a pp collision. Also, muons are expected to be
 1198 produced in the decay of several new particles; therefore, a good detection of muons
 1199 was on the leading principles when designing the CMS detector.

1200

1201 The CMS muon detection system is embedded in the return yoke as seen in figure
 1202 3.16. It is composed of three different detector types, the drift tube chambers (DT),
 1203 Cathode strip chambers (CSC), and resistive plate chambers (RPC); DT are located
 1204 in the central region $\eta < 1.2$ arranged in four layers of drift chambers filled with an
 1205 Ar/CO₂ gas mixture.

1206

1207 The muon endcaps are made of CSCs covering the region $\eta < 2.4$ and filled with a
 1208 mixture of Ar/CO₂/CF₄. The reason behind using a different detector type lies on
 1209 the different conditions in the forward region like the high muon rate and high resid-

1210 ual magnetic field.

1211

1212 The third type of detector used in the muon system is a set of four disks of RPCs
 1213 working in avalanche mode. The RPCs provide good spatial and time resolutions.
 1214 The track of $high - p_T$ muon candidates is built combining information from the
 1215 tracking system and the signal from up to six RPCs and four DT chambers.

1216 **3.3.8 CMS trigger system**

1217 Under normal conditions, CMS expects pp collisions every 25 ns  an interaction
 1218 rate of 40 MHz for which it is not possible to store the recorded data in full. In order
 1219 to handle this high event rate data, an online event selection, known as triggering, is
 1220 performed; triggering reduce the event rate to 100 Hz for storage and further offline
 1221 analysis.

1222

1223 The trigger system starts with a reduction of the event rate to 100 kHz in the so-called
 1224 “level 1 trigger (L1)”. L1 is based on dedicated programmable hardware like Field
 1225 Programmable Gate Arrays (FPGAs) and Application Specific Integrated Circuits
 1226 (ASICs), partly located in the detector itself; another portion is located in the CMS
 1227 under-ground cavern. Hit patterns information from the muon chambers and the en-
 1228 ergy deposits in the calorimeter are used to decide if an event is accepted or rejected,
 1229 according to selection requirements previously defined, which reflect the interesting
 1230 physics processes. Figure 3.17 shows the L1 trigger architecture 

1231

1232 The second stage in the trigger system is called “ high-level trigger (HLT)”; events
 1233 accepted by L1 are passed to HLT in order to make an initial reconstruction of them.

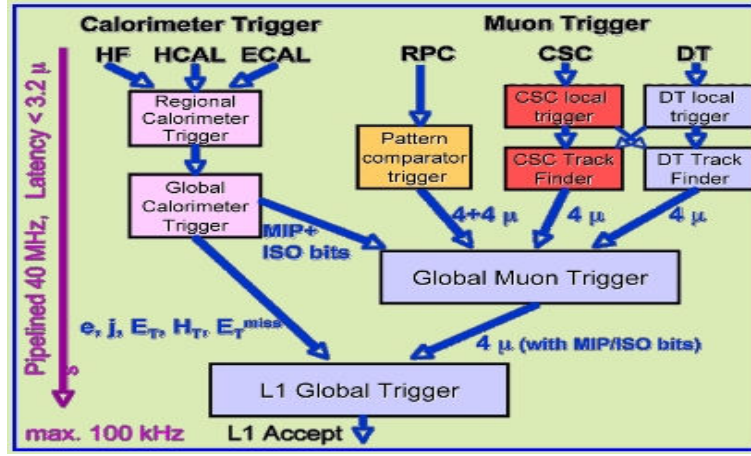


Figure 3.17: CMS Level-1 trigger architecture [76].

1234 HLT is software based and runs on a dedicated server farm, using selection algo-
 1235 rithms and high-level object definitions; the event rate at HLT is reduced to 100 Hz.
 1236 The first HLT stage takes information from the muon detectors and the calorimeters
 1237 to make the initial object reconstruction; in the next HLT stage, information from
 1238 the pixel and strip detectors is used to do first fast-tracking and then full tracking
 1239 online. This initial object reconstruction is used in further steps of the trigger system.

1240

1241 Events and preliminary reconstructed physics objects from HLT are sent to be fully
 1242 reconstructed at the CERN computing center. Again, the pixel detector information
 1243 provides high-quality seeds for the track reconstruction algorithm offline, primary ver-
 1244 tex reconstruction, electron and photon identification, muon reconstruction, τ iden-
 1245 tification, and b-tagging. After full reconstruction, data sets are made available for
 1246 offline analyses.

1247

1248 During the 2016-2017 technical stop, the L1 system was updated in order to improve
 1249 the physics object identification by improving the algorithms and accounting for the
 1250 increasing pile-up scenario.

1251 3.3.9 CMS computing

1252 After the data, coming from the experiment, are processed at several levels, they have
 1253 to be stored and made available for further analysis; in order to cope all the tasks
 1254 implied in the offline data processing, like transfer, simulation, reconstruction and
 1255 reprocessing, among others, a big computing power is required. The CMS computing
 1256 system is based on the distributed architecture concept, where users of the system
 1257 and physical computer centers are distributed worldwide and interconnected by high-
 1258 speed networks.

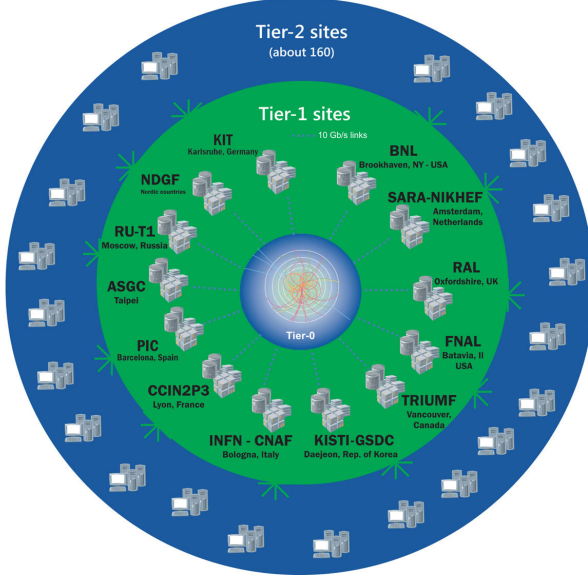


Figure 3.18: WLCG structure. The primary computer centers (Tier-0) are located at CERN (data center) and at the Wigner datacenter in Budapest. Tier-1 is composed of 13 centers and Tier-2 is composed of about 160 centers. [77].

1259 The worldwide LHC computing grid (WLCG) is the mechanism used to provide that
 1260 distributed environment. WLCG is a tiered structure connecting computing centers
 1261 around the world, which provides the necessary storage and computing facilities. The
 1262 primary computing centers of the WLCG are located at the CERN and the Wigner
 1263 datacenter in Budapest and are known as Tier-0 as shown in figure 3.18. The main

1264 responsibilities for each tier level are [77]

1265 • **Tier-0:** initial reconstruction of recorded events and storage of the resulting
1266 datasets, the distribution of raw data to the Tier-1 centers.

1267 • **Tier-1:** provide storage capacity, support for the Grid, safe-keeping of a pro-
1268 portional share of raw and reconstructed data, large-scale reprocessing and safe-
1269 keeping of corresponding output, generation of simulated events, distribution
1270 of data to Tier 2s, safe-keeping of a share of simulated data produced at these
1271 Tier 2s.

1272 • **Tier-2:** store sufficient data and provide adequate computing power for specific
1273 analysis tasks, provide analysis requirements and proportional share of simu-
1274 lated event production and reconstruction.

1275 Aside from the general computing strategy to manage the huge amount of data pro-
1276 duced by experiments, CMS uses a framework to perform a variety of processing,
1277 selection and analysis tasks. The central concept of the CMS data model is the
1278 “Event”; therefore, an event is the unit that contains the information from a single
1279 bunch crossing as well as any data derived from that information like the recon-
1280 structed objects, the details under which additional data are derived.

1281

1282 Events are passed as the input to the “physics modules” that obtain information from
1283 them and create new one; for instance, “event data producers” add new data into the
1284 events, “analyzers” produce an information summary from an event set, “filters” per-
1285 form selection and triggering.

1286

1287 CMS uses several event formats with different levels of detail and precision

- 1288 ● **Raw format:** events in this format contain the full recorded information from
1289 the detector as well as trigger decision and other metadata. An extended version
1290 of raw data is used to store information from the CMS Monte Carlo simulation
1291 tools. Raw data are stored permanently, occupying about 2MB/event
 - 1292 ● **RECO format:** events in this format correspond to raw data that have been
1293 submitted to reconstruction algorithms like primary and secondary vertex re-
1294 construction, particle ID, track-finding. RECO events contain physical objects
1295 and all the information used to reconstruct them; average size is about 0.5
1296 MB/event.
 - 1297 ● **AOD format:** Analysis Object Data (AOD) is the data format used in the
1298 physics analyses given that it contains the parameters describing the high-level
1299 physics objects in addition to enough information to allow a kinematic refitting if
1300 needed. AOD events are filtered versions of the RECO events to which skimming
1301 or other kind processes have been applied. Requires about 100 kB/event.
 - 1302 ● **Non-event data** are data needed to interpret and reconstruct events. Some
1303 of the non-event data used by CMS contains information about the detector
1304 contraction and condition data like calibrations, alignment, and detector status.
- 1305 Figure 3.19 shows the data flow scheme between CMS detector and hardware tiers.

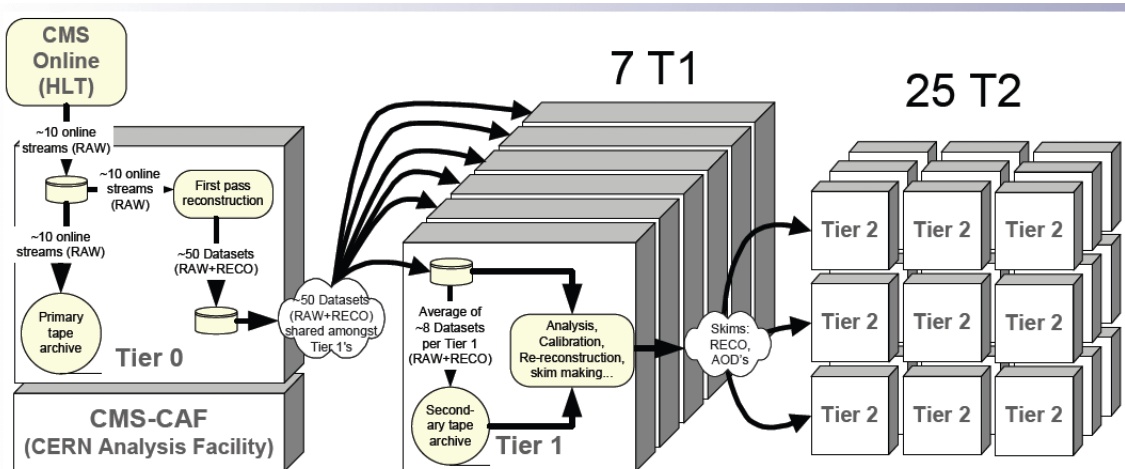


Figure 3.19: Data flow from CMS detector through hardware Tiers.

1306 **References**

- 1307 [1] J. Schwinger. “Quantum Electrodynamics. I. A Covariant Formulation”. Phys-
1308 ical Review. 74 (10): 1439-61, (1948).
- 1309 [2] R. P. Feynman. “Space-Time Approach to Quantum Electrodynamics”. Physical
1310 Review. 76 (6): 769-89, (1949).
- 1311 [3] S. Tomonaga. “On a Relativistically Invariant Formulation of the Quantum
1312 Theory of Wave Fields”. Progress of Theoretical Physics. 1 (2): 27-42, (1946).
- 1313 [4] D.J. Griffiths, “Introduction to electrodynamics”. 4th ed. Pearson, (2013).
- 1314 [5] F. Mandl, G. Shaw. “Quantum field theory.” Chichester: Wiley (2009).
- 1315 [6] F. Halzen, and A.D. Martin, “Quarks and leptons: An introductory course in
1316 modern particle physics”. New York: Wiley, (1984) .
- 1317 [7] File: Standard_Model_of_Elementary_Particle_dark.svg. (2017, June 12)
1318 Wikimedia Commons, the free media repository. Retrieved November
1319 27, 2017 from <https://www.collegiate-advanced-electricity.com/single-post/2017/04/10/The-Standard-Model-of-Particle-Physics>.
- 1321 [8] E. Noether, “Invariante Variationsprobleme”, Nachrichten von der Gesellschaft
1322 der Wissenschaften zu Göttingen, mathematisch-physikalische Klasse, vol. 1918,
1323 pp. 235-257, (1918).

- 1324 [9] C. Patrignani et al. (Particle Data Group), Chin. Phys. C, 40, 100001 (2016)
 1325 and 2017 update.
- 1326 [10] M. Goldhaber, L. Grodzins, A.W. Sunyar “Helicity of Neutrinos”, Phys. Rev.
 1327 109, 1015 (1958).
- 1328 [11] Palanque-Delabrouille N et al. “Neutrino masses and cosmology with Lyman-
 1329 alpha forest power spectrum”, JCAP 11 011 (2015).
- 1330 [12] M. Gell-Mann. “A Schematic Model of Baryons and Mesons”. Physics Letters.
 1331 8 (3): 214-215 (1964).
- 1332 [13] G. Zweig. “An SU(3) Model for Strong Interaction Symmetry and its Breaking”
 1333 (PDF). CERN Report No.8182/TH.401 (1964).
- 1334 [14] G. Zweig. “An SU(3) Model for Strong Interaction Symmetry and its Breaking:
 1335 II” (PDF). CERN Report No.8419/TH.412(1964).
- 1336 [15] M. Gell-Mann. “The Interpretation of the New Particles as Displaced Charged
 1337 Multiplets”. Il Nuovo Cimento 4: 848. (1956).
- 1338 [16] T. Nakano, K, Nishijima. “Charge Independence for V-particles”. Progress of
 1339 Theoretical Physics 10 (5): 581-582. (1953).
- 1340 [17] N. Cabibbo, “Unitary symmetry and leptonic decays” Physical Review Letters,
 1341 vol. 10, no. 12, p. 531, (1963).
- 1342 [18] M.Kobayashi, T.Maskawa, “CP-violation in the renormalizable theory of weak
 1343 interaction,” Progress of Theoretical Physics, vol. 49, no. 2, pp. 652-657, (1973).
- 1344 [19] File: Weak Decay (flipped).svg. (2017, June 12). Wikimedia Com-
 1345 mons, the free media repository. Retrieved November 27, 2017 from

- 1346 https://commons.wikimedia.org/w/index.php?title=File:Weak_Decay_(flipped)
1347 .svg&oldid=247498592.
- 1348 [20] Georgia Tech University. Coupling Constants for the Fundamental
1349 Forces(2005). Retrieved January 10, 2018, from http://hyperphysics.phy-
1350 astr.gsu.edu/hbase/Forces/couple.html#c2
- 1351 [21] M. Strassler. (May 31, 2013).The Strengths of the Known Forces. Retrieved Jan-
1352 uary 10, 2018, from https://profmattstrassler.com/articles-and-posts/particle-
1353 physics-basics/the-known-forces-of-nature/the-strength-of-the-known-forces/
- 1354 [22] S.L. Glashow. “Partial symmetries of weak interactions”, Nucl. Phys. 22 579-
1355 588, (1961).
- 1356 [23] A. Salam, J.C. Ward. “Electromagnetic and weak interactions”, Physics Letters
1357 13 168-171, (1964).
- 1358 [24] S. Weinberg, “A model of leptons”, Physical Review Letters, vol. 19, no. 21, p.
1359 1264, (1967).
- 1360 [25] M. Peskin, D. Schroeder, “An introduction to quantum field theory”. Perseus
1361 Books Publishing L.L.C., (1995).
- 1362 [26] A. Pich. “The Standard Model of Electroweak Interactions”
1363 https://arxiv.org/abs/1201.0537
- 1364 [27] F.Bellaiche. (2012, 2 September). “What’s this Higgs boson anyway?”. Retrieved
1365 from: https://www.quantum-bits.org/?p=233
- 1366 [28] M. Endres et al. Nature 487, 454-458 (2012) doi:10.1038/nature11255

- 1367 [29] F. Englert, R. Brout. “Broken Symmetry and the Mass of Gauge
 1368 Vector Mesons”. Physical Review Letters. 13 (9): 321-23.(1964)
 1369 doi:10.1103/PhysRevLett.13.321
- 1370 [30] P.Higgs. “Broken Symmetries and the Masses of Gauge Bosons”. Physical Re-
 1371 view Letters. 13 (16): 508-509,(1964). doi:10.1103/PhysRevLett.13.508.
- 1372 [31] G.Guralnik, C.R. Hagen and T.W.B. Kibble. “Global Conservation Laws
 1373 and Massless Particles”. Physical Review Letters. 13 (20): 585-587, (1964).
 1374 doi:10.1103/PhysRevLett.13.585.
- 1375 [32] CMS collaboration. “Observation of a new boson at a mass of 125 GeV with
 1376 the CMS experiment at the LHC”. Physics Letters B. 716 (1): 30-61 (2012).
 1377 arXiv:1207.7235. doi:10.1016/j.physletb.2012.08.021
- 1378 [33] ATLAS collaboration. “Observation of a New Particle in the Search for the Stan-
 1379 dard Model Higgs Boson with the ATLAS Detector at the LHC”. Physics Letters
 1380 B. 716 (1): 1-29 (2012). arXiv:1207.7214. doi:10.1016/j.physletb.2012.08.020.
- 1381 [34] ATLAS collaboration; CMS collaboration (26 March 2015). “Combined Mea-
 1382 surement of the Higgs Boson Mass in pp Collisions at $\sqrt{s}=7$ and 8 TeV with
 1383 the ATLAS and CMS Experiments”. Physical Review Letters. 114 (19): 191803.
 1384 arXiv:1503.07589. doi:10.1103/PhysRevLett.114.191803.
- 1385 [35] LHC InternationalMasterclasses“When protons collide”. Retrieved from
 1386 http://atlas.physicsmasterclasses.org/en/zpath_protoncollisions.htm
- 1387 [36] CMS Collaboration, “SM Higgs Branching Ratios and To-
 1388 tal Decay Widths (up-date in CERN Report4 2016)”).

- 1389 https://twiki.cern.ch/twiki/bin/view/LHCPhysics/CERNYellowReportPageBR
 1390 , last accessed on 17.12.2017.
- 1391 [37] R.Grant V. “Determination of Higgs branching ratios in $H \rightarrow W^+W^- \rightarrow l\nu jj$ and $H \rightarrow ZZ \rightarrow l^+l^-jj$ channels”. Physics Department, University of Tennessee (Dated: October 31, 2012). Retrieved from http://aesop.phys.utk.edu/ph611/2012/projects/Riley.pdf
- 1395 [38] LHC Higgs Cross Section Working Group, Denner, A., Heinemeyer, S. et al.
 1396 “Standard model Higgs-boson branching ratios with uncertainties”. Eur. Phys.
 1397 J. C (2011) 71: 1753. <https://doi.org/10.1140/epjc/s10052-011-1753-8>
- 1398 [39] F. Maltoni, K. Paul, T. Stelzer, and S. Willenbrock, “Associated production
 1399 of Higgs and single top at hadron colliders”, Phys.Rev. D64 (2001) 094023,
 1400 [hep-ph/0106293].
- 1401 [40] S. Biswas, E. Gabrielli, F. Margaroli, and B. Mele, “Direct constraints on the
 1402 top-Higgs coupling from the 8 TeV LHC data,” Journal of High Energy Physics,
 1403 vol. 07, p. 073, (2013).
- 1404 [41] M. Farina, C. Grojean, F. Maltoni, E. Salvioni, and A. Thamm, “Lifting de-
 1405 generacies in Higgs couplings using single top production in association with a
 1406 Higgs boson,” Journal of High Energy Physics, vol. 05, p. 022, (2013).
- 1407 [42] T.M. Tait and C.-P. Yuan, “Single top quark production as a window to physics
 1408 beyond the standard model”, Phys. Rev. D 63 (2000) 014018 [hep-ph/0007298].
- 1409 [43] F. Demartin, F. Maltoni, K. Mawatari, and M. Zaro, “Higgs production in
 1410 association with a single top quark at the LHC,” European Physical Journal C,
 1411 vol. 75, p. 267, (2015).

- 1412 [44] CMS Collaboration, “Modelling of the single top-quark pro-
 1413 duction in association with the Higgs boson at 13 TeV.”
 1414 <https://twiki.cern.ch/twiki/bin/viewauth/CMS/SingleTopHiggsGeneration13TeV>,
 1415 last accessed on 16.01.2018.
- 1416 [45] CMS Collaboration, “SM Higgs production cross sections at $\sqrt{s} = 13$ TeV.”
 1417 <https://twiki.cern.ch/twiki/bin/view/LHCPhysics/CERNYellowReportPageAt13TeV>, last
 1418 accessed on 16.01.2018.
- 1419 [46] S. Dawson, The effective W approximation, Nucl. Phys. B 249 (1985) 42.
- 1420 [47] S. Biswas, E. Gabrielli and B. Mele, JHEP 1301 (2013) 088 [[arXiv:1211.0499](https://arxiv.org/abs/1211.0499)
 1421 [hep-ph]].
- 1422 [48] F. Demartin, B. Maier, F. Maltoni, K. Mawatari, and M. Zaro, “tWH associated
 1423 production at the LHC”, European Physical Journal C, vol. 77, p. 34, (2017).
 1424 [arXiv:1607.05862](https://arxiv.org/abs/1607.05862)
- 1425 [49] LHC Higgs Cross Section Working Group, “Handbook of LHC Higgs Cross
 1426 Sections: 4.Deciphering the Nature of the Higgs Sector”, [arXiv:1610.07922](https://arxiv.org/abs/1610.07922).
- 1427 [50] J. Ellis, D. S. Hwang, K. Sakurai, and M. Takeuchi.“Disentangling Higgs-Top
 1428 Couplings in Associated Production”, JHEP 1404 (2014) 004, [[arXiv:1312.5736](https://arxiv.org/abs/1312.5736)].
- 1429 [51] CMS Collaboration, V. Khachatryan et al., “Precise determination of the mass
 1430 of the Higgs boson and tests of compatibility of its couplings with the standard
 1431 model predictions using proton collisions at 7 and 8 TeV,” [arXiv:1412.8662](https://arxiv.org/abs/1412.8662).
- 1432 [52] ATLAS and CMS Collaborations, “Measurements of the Higgs boson produc-
 1433 tion and decay rates and constraints on its couplings from a combined ATLAS

- 1434 and CMS analysis of the LHC pp collision data at $sqrts = 7$ and 8 TeV,” (2016).
- 1435 CERN-EP-2016-100, ATLAS-HIGG-2015-07, CMS-HIG-15-002.
- 1436 [53] File:Cern-accelerator-complex.svg. Wikimedia Commons,
 1437 the free media repository. Retrieved January, 2018 from
 1438 <https://commons.wikimedia.org/wiki/File:Cern-accelerator-complex.svg>
- 1439 [54] J.L. Caron , “Layout of the LEP tunnel including future LHC infrastructures.”,
 1440 (Nov, 1993). A C Collection. Legacy of AC. Pictures from 1992 to 2002. Re-
 1441 trieval from <https://cds.cern.ch/record/841542>
- 1442 [55] M. Vretenar, “The radio-frequency quadrupole”. CERN Yellow Report CERN-
 1443 2013-001, pp.207-223 DOI:10.5170/CERN-2013-001.207. arXiv:1303.6762
- 1444 [56] L.Evans. P. Bryant (editors). “LHC Machine”. JINST 3 S08001 (2008).
- 1445 [57] CERN Photographic Service.“Radio-frequency quadrupole, RFQ-1”, March
 1446 1983, CERN-AC-8303511. Retrieved from <https://cds.cern.ch/record/615852>.
- 1447 [58] CERN Photographic Service “Animation of CERN’s accelerator net-
 1448 work”, 14 October 2013. DOI: 10.17181/cds.1610170 Retrieved from
 1449 <https://videos.cern.ch/record/1610170>
- 1450 [59] C.Sutton. “Particle accelerator”.Encyclopedia Britannica. July 17, 2013. Re-
 1451 trieval from <https://www.britannica.com/technology/particle-accelerator>.
- 1452 [60] L.Guiraud. “Installation of LHC cavity in vacuum tank.”. July 27 2000. CERN-
 1453 AC-0007016. Retrieved from <https://cds.cern.ch/record/41567>.
- 1454 [61] J.L. Caron, “Magnetic field induced by the LHC dipole’s superconducting coils”.
 1455 March 1998. AC Collection. Legacy of AC. Pictures from 1992 to 2002. LHC-
 1456 PHO-1998-325. Retrieved from <https://cds.cern.ch/record/841511>

- 1457 [62] AC Team. “Diagram of an LHC dipole magnet”. June 1999. CERN-DI-9906025
1458 retrieved from <https://cds.cern.ch/record/40524>.
- 1459 [63] CMS Collaboration “Public CMS Luminosity Information”.
1460 <https://twiki.cern.ch/twiki/bin/view/CMSPublic/LumiPublicResults#2016>
1461 _proton_proton_13_TeV_collis, last accessed 24.01.2018
- 1462 [64] J.L Caron. “LHC Layout” AC Collection. Legacy of AC. Pictures
1463 from 1992 to 2002. September 1997, LHC-PHO-1997-060. Retrieved from
1464 <https://cds.cern.ch/record/841573>.
- 1465 [65] J.A. Coarasa. “The CMS Online Cluster: Setup, Operation and Maintenance
1466 of an Evolving Cluster”. ISGC 2012, 26 February - 2 March 2012, Academia
1467 Sinica, Taipei, Taiwan.
- 1468 [66] CMS Collaboration. “The CMS experiment at the CERN LHC” JINST 3 S08004
1469 (2008).
- 1470 [67] CMS Collaboration. “CMS detector drawings 2012” CMS-PHO-GEN-2012-002.
1471 Retrieved from <http://cds.cern.ch/record/1433717>.
- 1472 [68] R. Breedon. “View through the CMS detector during the cooldown of the
1473 solenoid on February 2006. CMS Collection”, February 2006, CMS-PHO-
1474 OREACH-2005-004, Retrieved from <https://cds.cern.ch/record/930094>.
- 1475 [69] A. Dominguez et. al. “CMS Technical Design Report for the Pixel Detector
1476 Upgrade”, CERN-LHCC-2012-016. CMS-TDR-11.
- 1477 [70] CMS Collaboration. “Description and performance of track and primary-vertex
1478 reconstruction with the CMS tracker,” Journal of Instrumentation, vol. 9, no.
1479 10, p. P10009,(2014).

- 1480 [71] CMS Collaboration and M. Brice. “Images of the CMS Tracker Inner
 1481 Barrel”, November 2008, CMS-PHO-TRACKER-2008-002. Retrieved from
 1482 <https://cds.cern.ch/record/1431467>.
- 1483 [72] M. Weber. “The CMS tracker”. 6th international conference on hyperons, charm
 1484 and beauty hadrons Chicago, June 28-July 3 2004.
- 1485 [73] CMS Collaboration. “Projected Performance of an Upgraded CMS Detector at
 1486 the LHC and HL-LHC: Contribution to the Snowmass Process”. Jul 26, 2013.
 1487 arXiv:1307.7135
- 1488 [74] L. Veillet. “End assembly of HB with EB rails and rotation in-
 1489 side SX ”,January 2002. CMS-PHO-HCAL-2002-002. Retrieved from
 1490 <https://cds.cern.ch/record/42594>.
- 1491 [75] J. Puerta-Pelayo.“First DT+RPC chambers installation round in the
 1492 UX5 cavern.”. January 2007, CMS-PHO-OREACH-2007-001. Retrieved from
 1493 <https://cds.cern.ch/record/1019185>
- 1494 [76] X. Cid Vidal and R. Cid Manzano. “CMS Global Muon Trigger” web
 1495 site: Taking a closer look at LHC. Retrieved from https://www.lhc-closer.es/taking_a_closer_look_at_lhc/0.lhc_trigger
- 1497 [77] WLCG Project Office, “Documents & Reference - Tiers - Structure,” (2014).
 1498 <http://wlcg.web.cern.ch/documents-reference> , last accessed on 30.01.2018.
- 1499 [78] CMS Collaboration, “Search for the associated production of a Higgs boson
 1500 with a single top quark in proton-proton collisions at $\sqrt{s} = 8$ TeV”, JHEP 06
 1501 (2016) 177,doi:10.1007/JHEP06(2016)177, arXiv:1509.08159.

- 1502 [79] B. Stieger, C. Jorda Lope et al., “Search for Associated Production of a Single
1503 Top Quark and a Higgs Boson in Leptonic Channels”, CMS Analysis Note CMS
1504 AN-14-140, 2014.
- 1505 [80] M. Peruzzi, C. Mueller, B. Stieger et al., “Search for ttH in multilepton final
1506 states at $\sqrt{s} = 13$ TeV”, CMS Analysis Note CMS AN-16-211, 2016.
- 1507 [81] CMS Collaboration, “Search for H to bbar in association with a single top quark
1508 as a test of Higgs boson couplings at $\sqrt{s} = 13$ TeV”, CMS Physics Analysis
1509 Summary CMS-PAS-HIG-16-019, 2016.
- 1510 [82] B. Maier, “SingleTopHiggProduction13TeV”, February, 2016.
1511 <https://twiki.cern.ch/twiki/bin/viewauth/CMS/SingleTopHiggsGeneration13TeV>.
- 1512 [83] M. Peruzzi, F. Romeo, B. Stieger et al., “Search for ttH in multilepton final1
1513 states at $\sqrt{s} = 13$ TeV”, CMS Analysis Note CMS AN-17-029, 2017.
- 1514 [84] B. WG, “BtagRecommendation80XReReco”, February, 2017.
1515 <https://twiki.cern.ch/twiki/bin/view/CMS/BtagRecommendation80XReReco>.